polymers

MDPI

Article

Hole Quality and Multi-Objective Optimisation in Dry Drilling of GLARE 3-3/2 Fibre Metal Laminates with HSS and Carbide Drills

Ömer Çağdaş Çınkır [1,*], Satılmış Ürgün [2,*], Sinan Fidan [1], Mustafa Özgür Bora [1], Mehmet İskender Özsoy [3] and Eser Yarar [4]

[1] Department of Aircraft Airframe and Powerplant Maintenance, Faculty of Aviation and Space Sciences, Kocaeli University, Kocaeli 41380, Türkiye; sfidan@kocaeli.edu.tr (S.F.); ozgur.bora@kocaeli.edu.tr (M.Ö.B.)
[2] Department of Aircraft Electrical and Electronics, Faculty of Aviation and Space Sciences, Kocaeli University, Kocaeli 41380, Türkiye
[3] Department of Mechanical Engineering, Faculty of Engineering, Sakarya University, Sakarya 54050, Türkiye; iozsoy@sakarya.edu.tr
[4] Department of Mechanical Engineering, Faculty of Engineering, Kocaeli University, Kocaeli 41380, Türkiye; eser.yarar@kocaeli.edu.tr
* Correspondence: o.cagdascinkir@gmail.com (Ö.Ç.Ç.); urgun@kocaeli.edu.tr (S.Ü.)

Abstract

Drilling of fibre metal laminates is difficult because the metal and composite layers respond differently to machining. This study aimed to identify the drill and cutting parameters that give the best dry-drilled holes in GLARE (glass laminate aluminium reinforced epoxy) 3-3/2. Rolled and ground high-speed steel drills (HSS-R, HSS-G) and a carbide-tipped drill were tested in a 3^3 full factorial design (715–3030 rpm; 0.1–0.3 mm/rev), with measurements of thrust force, infrared temperature, entry and exit surface topography and hole-wall morphology. Drill type governed the thrust force and feed governed the drill temperature, while the workpiece temperature did not exceed 43.4 °C. Exit burrs were the main defect, and their character depended on drill-specific speed–feed combinations. The carbide-tipped drill gave the most accurate holes and the cleanest walls but the largest exit burrs; the HSS-R drill caused bell-mouthed entries and fibre pull-out. Multi-objective optimisation of the measured conditions with a weighted desirability function identified the HSS-G drill at 1520 rpm and 0.1–0.2 mm/rev as the best operating window (at 0.2 mm/rev: D = 0.867, peak thrust force 31.1 N, exit burr height 1.8 µm). Independent confirmation experiments are required before production use.

Keywords: GLARE; fibre metal laminate; dry drilling; thrust force; burr height; bulging ratio; scanning electron microscopy; response surface methodology; desirability function

Check for updates

Academic Editor: Yunfa Zhang

Received: 22 October 2026
Revised: 6 November 2026
Accepted: 11 November 2026
Published: 13 November 2026

Copyright: © 2026 by the authors. Licensee MDPI, Basel, Switzerland. This article is an open access article distributed under the terms and conditions of the Creative Commons Attribution (CC BY) license.

1. Introduction

Fibre metal laminates (FMLs), in which thin metal sheets alternate with fibre-reinforced polymer (FRP) layers, combine the ductility of aluminium with the specific strength and fatigue resistance of composites [1]. GLARE (glass laminate aluminium reinforced epoxy), developed at Delft University of Technology and applied in the Airbus A380 fuselage, is the commercially most successful FML [2–5]: fibre bridging slows crack growth in the aluminium layers and improves the fatigue resistance and damage tolerance of the laminate [6–8]. Its production chain, from lay-up and curing to drilling and mechanical assembly, was described by Sinke [9], and the role of metal surface preparation was recently reviewed by Caggiano et al. [10].

Drilling is the most defect-prone step in the manufacture and repair of GLARE structures, because the aluminium and composite layers differ in cutting mechanics, thermal properties and damage modes. Recent reviews cover the machinability and sustainability of FMLs [11], one-shot drilling of FRP/aluminium stacks [12], machining of carbon-, glass- and natural-fibre composites [13], bibliometric trends in composite drilling [14], drilling of FRP [15], damage mechanisms in milling and grinding [16], advanced tools and coolants [17], finite-element modelling of composite machining [18] and the influence of hole quality on joint strength [19]. In a related study from the same laboratory, Ürgün et al. [20] combined thrust-force measurement, infrared thermography, optical profilometry and scanning electron microscopy (SEM) with factorial analysis of variance (ANOVA) to study dry drilling of carbon/glass-epoxy laminates on the same bench drilling machine.

Drilling-induced delamination occurs when the axial thrust force exceeds the interlaminar strength of the laminate. The fracture-mechanics model of Hocheng and Dharan [21] treats exit push-out and entry peel-up as separate events [22], and the delamination factor of Chen [23] remains the most common damage metric. Later work addressed the critical thrust force of different drill geometries [24,25], image-based delamination factors [26,27], the assessment and suppression of delamination [28,29] and the role of the chisel edge and step-drill geometry [30]; Ürgün et al. [20] showed experimentally that a stepped cutting profile produces a non-monotonic dependence of thrust and temperature on drill diameter.

Experimental work on GLARE drilling is dominated by the studies of Giasin et al., who quantified the effects of cutting speed and feed on thrust force, torque, roughness, burr formation, hole size and delamination [31,32], validated finite-element force predictions [33], and examined tool coatings [34,35], cryogenic and minimum-quantity-lubrication cooling [36,37] and ultrasonic assistance [38]. Other studies addressed force, torque, acoustic emission and delamination [39], drilling vs. helical milling [40], special drill geometries [41], process forces and temperature fields [42], hole quality and dust emission in GLARE 2B [43], cobalt high-speed-steel (HSS-Co) vs. carbide drills [44], carbon-fibre-reinforced aluminium laminates (CARALL) [45], Taguchi-based and machine-learning optimisation [46,47], regression modelling [48], ultrasonic-assisted drilling from the tool-design and simulation viewpoints [49,50], grey relational optimisation [51] and helical milling of CARALL [52].

Abrasive water-jet drilling has been proposed as an alternative to conventional drilling of GLARE [53–55]. Infrared thermography, as used here, was applied to GLARE drilling by Giasin and Ayvar-Soberanis [56] and by Ürgün et al. [20]; the merits of thermocouple and infrared measurements [57], the temperatures developed in drilling of carbon-fibre-reinforced polymers (CFRP) and their effect on the constituents [58–60] and the heat partition in CFRP cutting [61] have also been reported.

Design-of-experiments and optimisation techniques are widely used in composite and FML machining. Response-surface methodology (RSM) [62,63] combined with the desirability function of Derringer and Suich [64] is the standard multi-response approach and has been applied to burr height in drilling of aluminium-matrix composites [65,66], whereas FML drilling has relied mainly on Taguchi-based grey relational analysis [46,51]. Taguchi, regression and utility-theory approaches to drilling of glass-fibre-reinforced polymers (GFRP) and CFRP [67–71], evolutionary multi-objective algorithms [72], force–delamination correlations [73,74], nanocomposite milling [75] and numerous milling optimisation studies [76–83] follow the same pattern. Work on hybrid metal–composite stacks [84–87], tool wear and coatings [88,89], ultrasonic-assisted milling [90], Kevlar/epoxy milling [91], hand-laid-up hybrid laminates [92] and trimming-induced damage [93] provides further insight into the behaviour of the metal–composite interface.

Most of these studies consider a limited number of responses and describe hole damage with two-dimensional metrics such as the delamination factor or the wall roughness. Few studies measure the three-dimensional topography of both the entry and exit faces, fewer combine face metrics with SEM of the wall damage, and none compares rolled high-speed steel (HSS), ground HSS and carbide-tipped drills for GLARE 3-3/2 under dry conditions in a full factorial design with the categorical drill type included in a multi-objective optimisation. The present study therefore (i) measures the thrust force and the workpiece, chip and drill temperatures for three drills, three spindle speeds and three feeds; (ii) quantifies the entry and exit topography by non-contact profilometry and derives threshold-free aperture and edge metrics, namely burr height and bulging ratio; (iii) characterises the damage of the aluminium sheets, glass plies and adhesive layers on the hole walls by SEM; (iv) ranks the main and interaction effects by ANOVA and contribution analysis of replicated data; (v) identifies the best compromise of drill type, speed and feed by multi-objective optimisation of the measured conditions with a weighted desirability function and exhaustive grid search, with RSM used to describe the response trends; and (vi) derives practical recommendations for dry drilling of GLARE 3-3/2.

2. Materials and Methods

2.1. GLARE 3-3/2 Laminate

The GLARE 3-3/2 laminates consist of three plies of the 7075-T6 aluminium alloy material (thickness 0.41 mm [0.016 in]; part no. 7075T6-016x48x144AP) sandwiched together with two plies of glass fibre/epoxy composite material between them (Table 1). The composite layers include E-glass prepreg cloth certified according to Boeing Material Specification (BMS) 8-139 Class I (Style 1581, lot 92M0103414-031, Heatcon Composite Systems (Seattle, WA, USA); and Style 120, part no. BMS 8-139 120 38 CL1, lot 92M0104198-013, Pacific Coast Composites (Washington, WA, USA)) having the nominal weight per cent of the resin content 36% in Style 1581 according to the vendor data [94].

Table 1. Constituents of the GLARE 3-3/2 laminate.

Layer	Material	Specification/Part No.	Thickness
Aluminium sheets (×3)	7075-T6	7075T6-016x48x144AP	0.41 mm (0.016 in, nominal)
Glass/epoxy layers (×2)	E-glass prepreg, Style 1581 (36 wt % resin) and Style 120	BMS 8-139 Class I (Heatcon/Pacific Coast Composites)	[layer thickness/number of prepreg plies per layer]
Adhesive	3M Scotch-Weld AF 163-2 film adhesive	—	—
Cure	Autoclave, 105 ± 5 °C, 6 h, 1.2 bar, vacuum 0.15 bar	Airbus Structural Repair Manual (SRM) 53-15-12	Total 2.55 mm (digital calliper)

The aluminium sheets were prepared by cutting them to the required sizes and treating them with a degreasing process and primer treatment. Then, the sheets were bonded using 3M Scotch-Weld AF 163-2 (Saint Paul, MN, USA) film adhesive and laminated using the prepreg layers. The laminating process included applying the peel ply and breather to the lay-up, and vacuum-bagging and curing of the lay-up in an autoclave according to the cycle recommended for the GLARE panels in the Airbus Structural Repair Manual 53-15-12 [95]. The curing cycle consisted of a vacuum of 0.15 ± 0.05 bar, an autoclave pressure increase to 1.2 bar in steps, heating to 105 ± 5 °C at 1.5 °C/min, and a 6 h dwell.

2.2. Drilling Set-Up and Experimental Design

The dry drilling operations were performed on a Toss United TU5032B bench drilling machine (Nantong Sieg Machinery Co., Ltd., Haimen, China). This machine is equipped with fixed steps of spindle speed due to its step-pulley drive, and mechanical feed increments of 0.1, 0.2, and 0.3 mm/rev. The same machine was used in the related work by Ürgün et al. [20] because of the stable cutting conditions. The 3 × 3 × 3 full-factorial design was designed using three different spindle speeds (715, 1520, and 3030 rpm), three feed rates (0.1, 0.2, and 0.3 mm/rev) and three different drill types, resulting in 27 conditions. The specimens were clamped into the fixture mounted on the dynamometer, which in turn was clamped to the machine table. The three drills that were tested in this work were: (a) rolled (not ground) DIN 338 high-speed-steel twist drill (HSS-R, Ø6.00 mm), (b) completely ground DIN 338 high-speed-steel twist drill (HSS-G, Ø6.00 mm), and (c) carbide-tipped twist drill with Ø6.35 mm (1/4 in) diameter. All the drills had a point angle of 118°. Every drill was new and was used for drilling nine holes in its group, and no noticeable wear of the cutting edges was found after nine holes. Thermal measurements were performed using a FLIR A325sc infrared camera (Teledyne FLIR, Wilsonville, OR, USA) positioned 50 cm from the drilling zone, with an emissivity setting of 0.90. Measurement parameters were configured using the camera software. Since surface emissivity, reflected radiation, and spatial resolution may affect measurement accuracy, and independent calibration and uncertainty quantification were not performed, the recorded values are reported as apparent temperatures and interpreted primarily for comparative analysis of thermal behaviour. The whole data set is represented by three independent experimental sets of the 3 × 3 × 3 design (N = 81 observations). Each group of samples was drilled by means of a new drill of the corresponding type on a different specimen. All the drills used for a particular group were from the same batch, while the specimens came from the same autoclaved laminate panel. All holes were drilled using the same machine, the same holder, and the same operator. Thus, the three groups are within-batch replicates, and their scatter shows how repeatable the drilling-measuring procedure is under these constant conditions. The first experimental set (odd specimens E1–E53, 27 holes; Table 2) was used for the hole-by-hole analysis that is described in Sections 3.1–3.5, and all three experimental sets were used in the contribution analysis and multi-objective optimisation that is described in Section 3.6 (means for the conditions are presented in Table S1).

Table 2. Experimental matrix of the first series (3^3 full factorial, 27 holes) and measured responses. F_{mean}, F_{max}: mean and maximum thrust force; T_w: workpiece surface temperature (point 2); T_{chip}: maximum chip temperature; T_{max}: maximum drill temperature; D_{eq}: aperture equivalent diameter at the entry (in) and exit (out) face; BH_{in}, BH_{out}: burr height at the entry and exit face; BR_{out}: bulging ratio of the 0–300 µm exit edge band. † Chip packing around the drill point recorded during the test; E9 is excluded from the face-metric statistics in Sections 3.3 and 3.5 but retained in the force and temperature analyses, and E45 is retained in all analyses (Section 2.6; Table S6).

Exp.	Drill	n (rpm)	f (mm/rev)	F_{mean} (N)	F_{max} (N)	T_w (°C)	T_{chip} (°C)	T_{max} (°C)	$D_{eq,in}$ (mm)	$D_{eq,out}$ (mm)	BH_{in} (µm)	BH_{out} (µm)	BR_{out} (%)
E1	HSS-R	715	0.1	39.0	39.6	25.8	43.4	96.5	6.41	6.02	14	17	11.1
E7	HSS-R	715	0.2	32.9	33.3	24.2	31.0	100.5	6.39	6.00	6	38	13.7
E13	HSS-R	715	0.3	35.0	35.7	26.2	43.0	112.4	6.37	6.04	4	28	8.0
E19	HSS-R	1520	0.1	35.6	36.8	26.7	54.0	102.6	6.16	6.04	9	12	1.2
E25	HSS-R	1520	0.2	35.6	37.0	26.5	71.2	112.9	6.03	6.04	−75	21	3.8
E31	HSS-R	1520	0.3	37.5	38.0	27.2	82.0	119.3	6.08	5.97	−6	32	5.8
E37	HSS-R	3030	0.1	34.2	34.6	28.5	47.7	114.2	6.47	6.10	2	24	9.8
E43	HSS-R	3030	0.2	40.5	41.0	29.3	32.4	100.7	6.35	6.05	7	20	1.4

Table 2. *Cont.*

Exp.	Drill	n (rpm)	f (mm/rev)	F_{mean} (N)	F_{max} (N)	T_w (°C)	T_{chip} (°C)	T_{max} (°C)	$D_{eq,in}$ (mm)	$D_{eq,out}$ (mm)	BH_{in} (µm)	BH_{out} (µm)	BR_{out} (%)
E49	HSS-R	3030	0.3	42.1	43.5	30.0	81.7	107.6	6.44	6.09	−25	−23	0.1
E3	HSS-G	715	0.1	34.5	37.1	31.9	56.9	84.4	5.95	5.89	3	26	5.1
E9 †	HSS-G	715	0.2	43.6	46.1	33.0	85.2	104.3	6.01	7.00	21	245	85.1
E15	HSS-G	715	0.3	31.6	34.0	28.6	66.2	123.0	5.93	5.99	7	8	2.7
E21	HSS-G	1520	0.1	28.5	29.4	26.5	34.8	111.8	6.01	5.98	−12	23	0.4
E27	HSS-G	1520	0.2	30.9	31.9	29.1	37.5	106.2	5.96	6.00	−12	2	0.8
E33	HSS-G	1520	0.3	28.9	29.6	27.0	33.8	107.6	6.01	6.00	7	16	4.5
E39	HSS-G	3030	0.1	29.7	30.2	28.3	59.1	106.9	6.02	6.00	19	23	4.6
E45 †	HSS-G	3030	0.2	41.9	46.2	43.4	82.3	99.2	6.03	5.97	1	22	6.4
E51	HSS-G	3030	0.3	30.4	31.1	29.0	70.6	120.3	6.02	6.02	−1	27	5.2
E5	Carbide	715	0.1	35.2	37.6	26.3	32.8	89.1	6.39	6.35	28	42	19.3
E11	Carbide	715	0.2	44.0	47.0	37.8	85.6	104.3	6.41	6.35	37	−71	6.3
E17	Carbide	715	0.3	39.4	41.7	31.2	66.7	112.5	6.43	6.31	24	75	32.7
E23	Carbide	1520	0.1	40.7	42.5	37.9	55.6	106.8	6.36	6.37	−11	91	23.4
E29	Carbide	1520	0.2	37.9	38.6	29.9	41.2	114.4	6.40	6.36	15	59	26.0
E35	Carbide	1520	0.3	36.8	37.6	29.8	74.1	119.8	6.31	6.35	−11	152	41.5
E41	Carbide	3030	0.1	40.6	41.3	30.5	26.1	101.5	6.37	6.34	−15	−41	10.5
E47	Carbide	3030	0.2	36.7	37.9	30.5	43.2	108.8	6.39	6.34	−92	12	31.4
E53	Carbide	3030	0.3	43.9	44.8	34.4	58.8	109.3	6.31	6.33	−25	34	10.8

2.3. Thrust Force and Temperature Measurement

The axial thrust force was measured using a Kistler 9272 four-component piezoelectric dynamometer and a charge amplifier, Kistler 5070A (Kistler Group, Winterthur, Switzerland). Data acquisition was done with the use of DynoWare 2825D-02. For each hole, the following parameters were calculated: mean thrust force (F_{mean}) and maximum thrust force (F_{max}). Torque was not measured. Drilling zone temperature was measured simultaneously using a FLIR A325sc infrared camera (320 × 240 pixels, 7.5–13 µm) placed 50 cm away from the workpiece and oriented at 60° to it, with recordings analysed using FLIR ResearchIR software; such an arrangement was also applied by Ürgün et al. [20]. The workpiece temperature (T_w) and chip temperature (T_{chip}) were determined by averaging the apparent temperature values of the pixels within the corresponding workpiece and chip measurement regions, respectively. The maximum temperature (T_{max}) was defined as the highest apparent temperature recorded throughout the drilling process. Thermal images captured at the moment of drill withdrawal were additionally used to illustrate the temperature distribution under selected cutting conditions. Moreover, single images obtained at the moment of drill withdrawal were analysed under certain conditions (see Section 3.2).

2.4. Hole-Edge Topography at the Entry and Exit Faces

Quantification of the topography of the entrance (drill entry) and exit (drill breakout) was done with a Nanovea PS-50 optical profilometer (non-contact chromatic confocal sensor). In each hole, scanning of a 10 mm × 10 mm square area centred on the hole was performed with a lateral step size of 15 µm in the x direction and 20 µm in the y direction, resulting in 668 × 501 height points for each face. Levelling of the height maps was done by least-squares fitting of a flat surface in an undamaged annulus between 4.2 and 4.9 mm

radii from the centre of the hole, after 3σ outlier rejection, which results in a relative height profile with respect to the intact surface of the sheet.

Each face was scanned from outside the laminate, and the levelled height $z^*(x, y)$ is therefore positive outwards at both faces:

$$z^*(x, y) = z(x, y) - (a + bx + cy) \quad (1)$$

where a, b and c were obtained by least-squares fitting to the points of the annulus 4.2 mm $\leq r \leq$ 4.9 mm after 3σ outlier rejection. Points in the through-hole and on near-vertical surfaces return no signal. The aperture Ω was defined as the largest connected region of non-measured points; its area A is the number of points in Ω multiplied by the pixel area (15 µm × 20 µm), and its centroid (x_c, y_c) was taken as the hole centre. The equivalent diameter is the diameter of the circle with the same area:

$$D_{eq} = 2(A/\pi)\text{^}(1/2), \quad (2)$$

The aperture boundary was located along 180 radial rays $\theta_k = 2\pi k/180$ (k = 0, ..., 179) emanating from the centroid, giving the boundary radius $R(\theta_k)$. The out-of-roundness was calculated from the 90 diametral chords through the centroid:

$$D_{max} - D_{min} = \max_j [R(\theta_j) + R(\theta_j + \pi)] - \min_j [R(\theta_j) + R(\theta_j + \pi)], j = 0, ..., 89. \quad (3)$$

Edge quality was evaluated along the same 180 rays. On each ray, the levelled height was sampled by bilinear interpolation as a function of the distance s from the boundary, $h_k(s) = z^*[x_c + (R(\theta_k) + s) \cos \theta_k, y_c + (R(\theta_k) + s) \sin \theta_k]$, at a step of Δs for $0 \leq s \leq$ 300 µm. The circumferentially averaged hole-edge height profile at the entry face, $h^-(s) = (1/180)\ \Sigma_k\ h_k(s))$, was obtained by averaging the height profiles over all 180 radial rays. Three metrics were derived from these samples, using only valid (measured) points:

$$BH = \text{mean}\{h_k(s)\text{: } 0 \leq s \leq 60\ \mu m, k = 0, ..., 179\}, \quad (4)$$

The bulging ratio and the depressed fraction were evaluated on the pixels of the edge band. For each valid pixel, the distance d to the aperture was obtained by a Euclidean distance transform that accounts for the anisotropic pixel size (15 µm × 20 µm), and

$$BR(t) = 100 \cdot N[z^* > +t]/N_{band}, DF(t) = 100 \cdot N[z^* < -t]/N_{band}, 0 < d \leq 300\ \mu m, t = 40\ \mu m, \quad (5)$$

where N is the number of valid band pixels that satisfy the condition, and N_{band} is the number of valid pixels in the 0–300 µm band.

The burr height BH (BH_{in} and BH_{out} at the entry and exit faces) is thus the mean height of the 60 µm-wide zone adjacent to the wall, corresponding to three to four lateral sampling steps. Because the sign convention is identical at both faces, a positive BH denotes material protruding beyond the original face and a negative BH denotes an edge lying inside the laminate, i.e., below the original surface at the entry and above it at the exit (Figure 1a). The bulging ratio BR and the depressed fraction DF (BR_{in}, BR_{out}, DF_{in} and DF_{out}) are the percentages of the 0–300 µm edge band lying more than 40 µm above and below the reference plane, respectively, and quantify the circumferential extent of the raised and depressed parts of the edge [21,96]. The threshold t = 40 µm was chosen primarily due to two considerations. Firstly, it is well above the noise values encountered with respect to measurements and levelling. For the levelling annulus, the median RMS scatter of height is 2.5 µm (52 regular faces, range 1.1–5.3 µm), the median 99.9th percentile value of $|z^*|$ is 9.3 µm, and on average only 0.02% (up to 0.22% maximum) of the pixels exceed ±40 µm. Therefore, the detection of a band pixel exceeding the threshold t can be reliably considered an effect of drilling-induced

deformation and not measurement noise, sheet waviness, or levelling errors. Secondly, 40 µm equals roughly 10% of sheet thickness (0.41 mm); hence, both BR and DF detect deformations of the sheet at a scale corresponding to those observed with the HSS drills. Recognising the arbitrary nature of using any threshold value, the analysis was also conducted for t = 20, 30, 50, 60, and 80 µm (Section 3.3; Table S7, Figure S10). Due to the fact that the chromatic confocal sensor cannot detect any surface outside its acceptance angle, highly rounded, chipped, and folded edges can be partly covered by the unmeasured aperture; thus, the negative BH provides an underestimation of the edge depression.

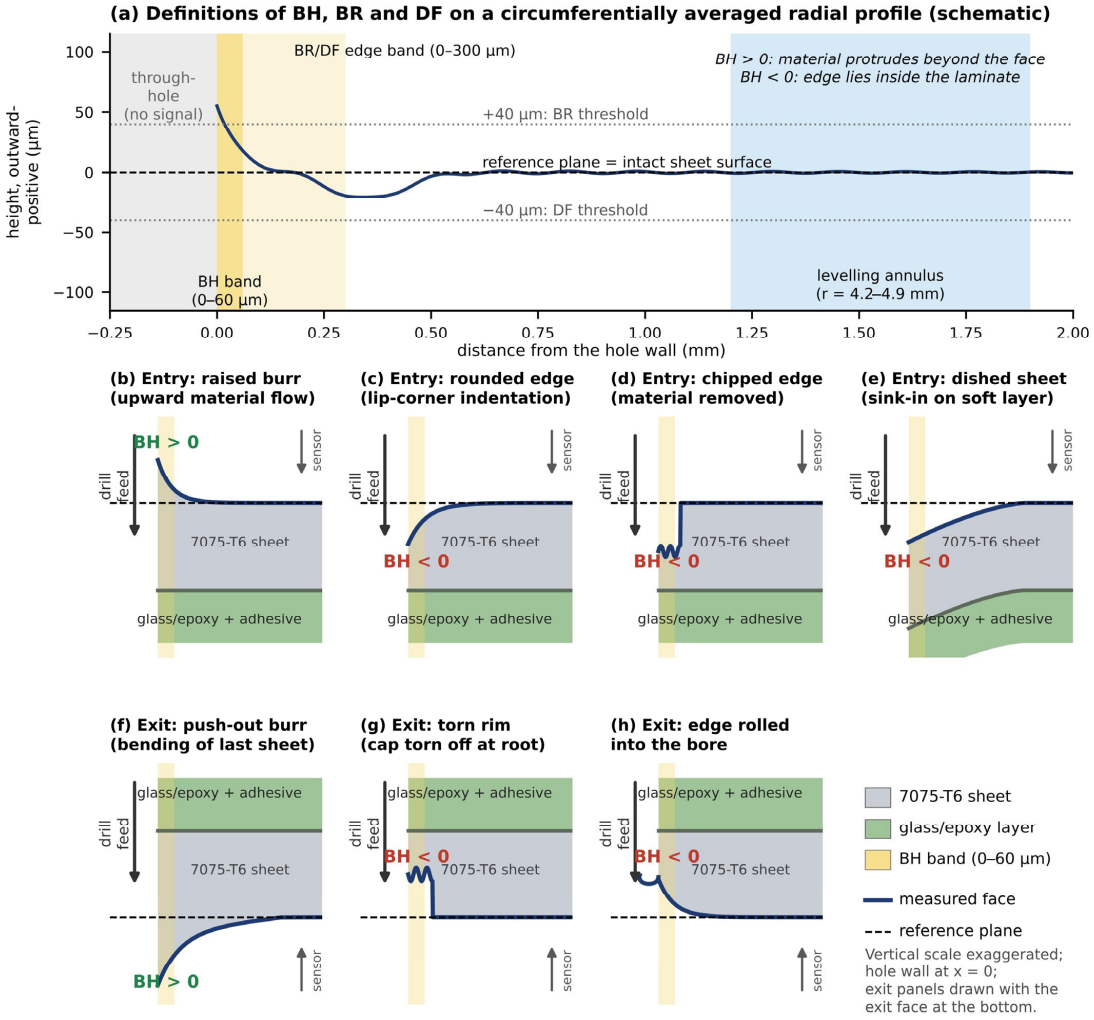


Figure 1. Schematic definition and physical meaning of the edge metrics. (**a**) Circumferentially averaged radial height profile with the 0–60 µm burr-height band, the 0–300 µm edge band used for the bulging ratio (BR, more than 40 µm above the reference plane) and the depressed fraction (DF, more than 40 µm below), and the levelling annulus (r = 4.2–4.9 mm; distances from the wall given for the Ø6.00 mm holes); heights are outward-positive at both faces. (**b**–**e**) Entry face: (**b**) raised edge formed by peel-up (BH > 0); (**c**) edge rounded by indentation of the lip corners; (**d**) chipped or torn edge; and (**e**) dishing of the top sheet on the compliant glass/epoxy layer (BH < 0). (**f**–**h**) Exit face, drawn with the exit face at the bottom: (**f**) push-out burr formed by bending of the last sheet (BH > 0); (**g**) torn rim left by a cap separated at its root; and (**h**) edge rolled into the bore (BH < 0). Vertical scale exaggerated.

The introduced metrics possess certain differences from conventional hole quality assessment parameters in a number of aspects. The burr heights measured with the stylus, height gauge, and optical microscope are usually performed at a few points along the

circumference (usually, four to eight) and are provided as the maximum value above the surface [32,34,96]. On the other hand, burr height (BH) is defined as a mean value within a specified 60 µm region and is measured for 180 orientations and, therefore, is less sensitive to individual peaks and usually provides a smaller value compared to maximum burr height. Thus, absolute BH values should be treated in the context of literature data. The bulging ratio (BR) and the depressed fraction (DF) do not have any analogues among the conventional burr measurements and could be compared to an area-based (adjusted) delamination factor [26]. Like the latter, BR and DF assess the extent of the damaged zone and not the maximum value of the damage, whereas in the traditional $F_d = D_{max}/D_0$ [23], the maximum radial extent of the damaged zone is considered.

The metric D_{eq} characterises the opening of the hole on both faces and represents the diameter of the hole measured by the coordinate measuring machine (CMM) or the bore gauge [32,35] only for a perfectly cylindrical wall. Any bell-mouthed entry or burrs inside the bore increase the D_{eq} value without changing the diameter in the middle of the laminate. Finally, the diametral out-of-roundness parameter provided by Equation (3) approximately equals twice the least-squares-circle roundness (peak-to-valley radial deviation) used in CMM form error assessments [35] for oval, two-lobed holes but does not capture odd-lobed errors. Since this parameter is measured at the aperture border, it also includes individual burrs and chip pieces.

In addition, the surface descriptors 'Hole' and 'Peak' measured by the software of the instrument (Professional 3D 6.2, ISO 25178 [97] particle analysis) were also evaluated for comparative purposes. Areal roughness parameters Sa and Sz were not used as hole-quality measures because they are dominated by the aperture itself in a through-hole scan.

2.5. Scanning Electron Microscopy of the Hole Walls

After profilometric measurement, twelve samples from the first set of holes were cut along the plane cutting the hole axis, and their walls were inspected using a JEOL JSM-6060 scanning electron microscope (JEOL Ltd., Tokyo, Japan) operated at 15 kV acceleration voltage and a working distance of 24 mm. Holes drilled with the HSS-R and carbide drills at 0.1 and 0.3 mm/rev feed rates and at the three spindle speeds were chosen (E1, E13, E19, E31, E37, and E49 for HSS-R; E5, E17, E23, E35, E41, and E53 for carbide; Table 2). These correspond to the two drills having the most contrasting entry- and exit-face characteristics at the two extreme feed rates. The ground HSS drill was not considered in the SEM investigations. For each hole, an overall backscattered-electron (BES) micrograph (×20 magnification) of the hole wall was taken, followed by BES images at ×100 magnification in several positions across the thickness. Additional secondary-electron (SEI) images were made for the carbide hole at 715 rpm/0.1 mm/rev. In BES images, Z-contrast allows for distinguishing 7075-T6 sheets (white), glass-fibre plies (light grey with identifiable fibre bundles), and epoxy-rich adhesive interlayers (dark grey). This makes it possible to identify layer boundaries, aluminium shavings and glass fibres without etching. Damage characteristics were described as feed marks, aluminium sheet ploughing and smearing, fibre pull-out, fibre fracture, matrix smearing, matrix chip-off or tearing, interfacial delamination and adhered chips and debris, following the classification used for FRP and FML hole walls [11,12,15,16].

2.6. Statistical Analysis and Multi-Objective Optimisation

Responses in the initial experiment were subjected to analysis by the three-factor ANOVA with fixed categorical factors of drill type, spindle speed, and feed, as well as the three two-factor interactions. Due to the unreplicated nature of this design, the three-factor interaction played the role of the error term in the test statistics, and the type-II sums of

squares provided percentage contributions to the sum of squares of each term. As for edge quality measures that demonstrated severe skewness, the non-parametric Kruskal–Wallis test and Wilcoxon signed-rank test were applied. Correlations between the responses were measured by Pearson and Spearman methods. Effect sizes are reported together with the *p*-values: ω^2 for the ANOVA terms (negative estimates set to zero), $\varepsilon^2 = H/(N - 1)$ for the Kruskal–Wallis test and $r = Z/\sqrt{N}$ for the Wilcoxon signed-rank test, together with the Hodges–Lehmann estimate of the median difference and its 95% confidence interval (CI). Group means are given with 95% t-based CIs and correlation coefficients with 95% CIs from the Fisher z-transformation (bootstrap percentile CI for Spearman's ρ). Skewed edge metrics are additionally summarised by the median and interquartile range (IQR). The significance level was set at $\alpha = 0.05$. Chip packing at the drill point was recorded for two holes in the first series: E9 and E45 (HSS-G, 0.2 mm/rev; Table 2). A single criterion was used: a hole was removed from the analysis if the process failure resulted in the measured parameter exceeding the range of the nominal cutting mechanism. Chip packing is an intrinsic property of dry drilling affecting the thrust force and temperature; thus, both E9 and E45 were kept in all the process-response analyses (Sections 3.1 and 3.2; Table 3—F_{mean}, T_{max} and T_{chip}). The exit face of E45 was geometrically regular (BH_{out} = 22 µm, BRout = 6.4%), whereas the exit face of E9 was circumferentially bent (BH_{out} = 245 µm, BR_{out} = 85.1%, out-of-roundness = 4.0 mm, effective exit diameter = 7.0 mm), indicating that the face was punched, not drilled. Nevertheless, E9 and E45 are listed in Table 2. In the replicated data set (Section 3.6), the chip-clogged condition corresponding to E9 (HSS-G, 715 rpm, 0.2 mm/rev) was kept in the contribution analysis, response-surface models and optimisation, as the multi-objective optimisation needs to be penalised by such conditions; the impact of E9 was evaluated using a sensitivity analysis (Section 3.6.1). If any exclusion affected the result, the value including E9 is also listed. A list of E9 and E45 handling in every analysis is presented in Table S6.

Table 3. ANOVA of the process responses of the first series (27 holes; type-II sums of squares; PC = percentage contribution; three-factor interaction pooled as error). F_(mean), T_(max) and T_(chip): all 27 holes (E9 and E45 included); BR_(out): 26 holes, E9 excluded (seven error degrees of freedom; Section 2.6). Values of $p < 0.05$ are significant.

Source	F_{mean} PC (%)	*p*	$F_{mean}\omega^2$	T_{max} PC (%)	*p*	$T_{max}\omega^2$	T_{chip} PC (%)	*p*	$T_{chip}\omega^2$	BR_{out} PC (%)	*p*	$BR_{out}\ \omega^2$
Drill type	29.6	0.029	0.24	0.0	0.994	0.00	1.3	0.725	0.00	57.8	0.003	0.53
Spindle speed	8.4	0.258	0.03	14.5	0.095	0.10	0.4	0.898	0.00	1.5	0.709	0.00
Feed	6.9	0.318	0.02	38.0	0.011	0.33	16.5	0.058	0.12	1.2	0.748	0.00
Drill × Speed	9.4	0.505	0.00	2.5	0.886	0.00	45.5	0.018	0.37	11.8	0.313	0.04
Drill × Feed	18.1	0.232	0.08	5.9	0.643	0.00	12.7	0.265	0.05	4.8	0.682	0.00
Speed × Feed	7.0	0.626	0.00	21.0	0.144	0.12	7.6	0.480	0.00	8.8	0.435	0.01
Error	20.7	—	—	18.1	—	—	15.9	—	—	14.2	—	—

For the replicated data (N = 81), the complete 3^3 design, including the three-factor interaction, was used, with 54 degrees of freedom for the error term and the contribution of each term expressed in terms of its percentage of the total sum of squares. Due to the fact that this error term is mostly an indicator of the repeatability within the batch (Section 2.2), the *p*-values of the replicated model were not used to ascertain the practical importance of the effects. The contribution was rather compared with those in the unreplicated 27-holes ANOVA, where the three-factor interaction results in a greater variance estimate. Pooled second-order response-surface models [62,63] with intercepts specific to each drill were

estimated next. The optimisation was performed on the measured condition means; the response-surface models were used to describe the effects of speed and feed, and their predictions were not used to select the recommended condition, as their cross-validated R^2 was negative. The optimal settings of drill type, spindle speed, and feed were obtained by maximising a weighted desirability function [64] through exhaustive grid search and leave-one-condition-out cross-validation, stratified bootstrap resampling [98], other weighting schemes, and weighted-sum score [99]. The method is outlined in Section 3.6. All computations were done in Python 3.13 (NumPy 2.5.3, SciPy 1.18.1, pandas 3.0.5, statsmodels 0.15.0, Matplotlib 3.11.2).

3. Results and Discussion

3.1. Thrust Force

The mean and peak thrust forces of the 27 holes are listed in Table 2 and plotted in Figure 2a,b. The mean thrust force ranged from 28.5 N (HSS-G, 1520 rpm, 0.1 mm/rev) to 44.0 N (carbide, 715 rpm, 0.2 mm/rev), and the peak force exceeded the mean by only 0.4–2.6 N, indicating a stable cut without force spikes at the aluminium/composite interfaces. The drill averages over all nine holes, including the chip-packed holes E9 and E45 (Section 2.6), were 33.3 ± 5.6 N (HSS-G; 95% CI 29.0–37.7 N), 36.9 ± 3.1 N (HSS-R; 34.6–39.3 N) and 39.5 ± 3.1 N (carbide; 37.1–41.9 N). The two highest HSS-G values (43.6 N in E9 and 41.9 N in E45) coincided with chip packing around the drill point; without them, the HSS-G mean falls to 30.6 N, 17% below HSS-R and 23% below carbide. The higher thrust of the carbide drill is attributed to its larger diameter (6.35 vs. 6.00 mm, i.e., a 12% longer chisel edge) and to the less acute cutting edge of a wear-resistant carbide grade.

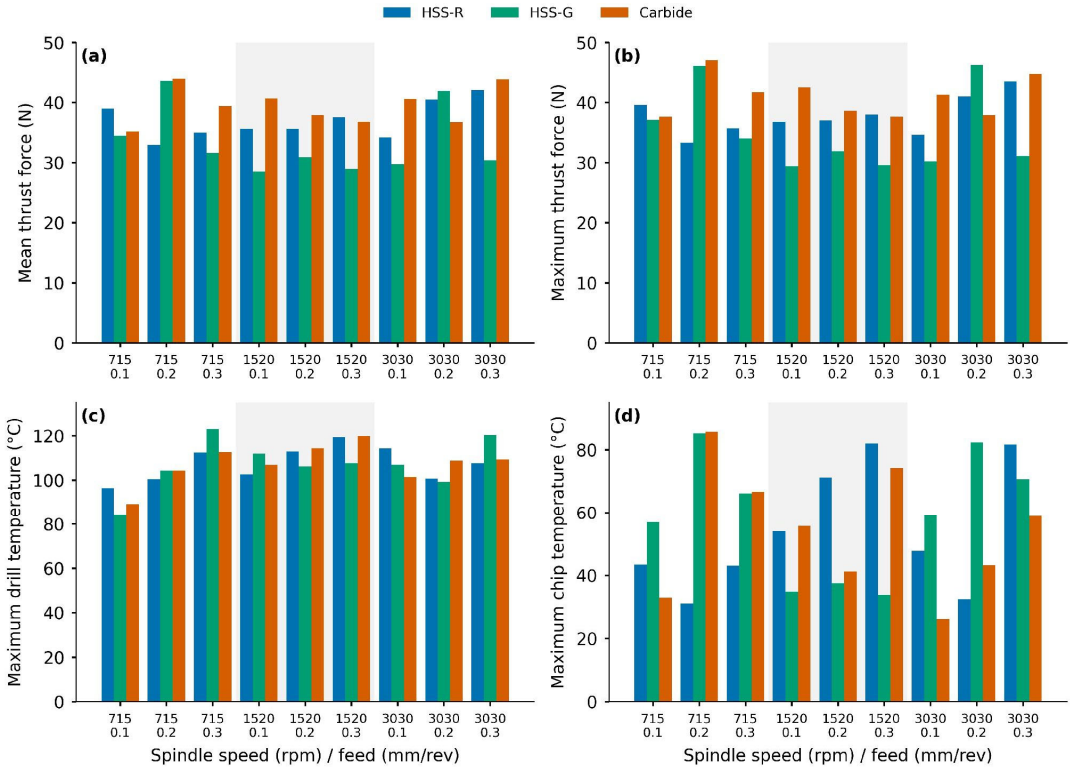


Figure 2. (**a**) Mean and (**b**) maximum thrust force, (**c**) maximum drill temperature and (**d**) maximum chip temperature for the three drills at each spindle-speed/feed combination (first series, 27 holes; the 1520 rpm group is shaded). The chip-packed holes E9 and E45 (HSS-G, 0.2 mm/rev) are included.

The ANOVA (Table 3) identifies drill type as the only significant factor for the mean thrust force ($p = 0.014$ in the main-effects model; 29.6% contribution; $\omega^2 = 0.24$), whereas spindle speed (8.4%), feed (6.9%) and the interactions are not significant. The main-effect plots (Figure S1a) show a shallow minimum at 1520 rpm and a maximum at 0.2 mm/rev, but these effects (about 3 N) are comparable with the residual scatter. The weak feed effect, in contrast to drilling of thicker GLARE on computer numerical control (CNC) machining centres [31,32,43], is explained by the small laminate thickness (2.55 mm, of which only 1.2 mm is aluminium), so that the chisel edge never engages more than one layer at a time, and by the mechanically coupled feed of the bench drilling machine. The thrust forces (28–44 N) are far below the 150–500 N reported for 6 mm holes in 3–5 mm thick GLARE [31,42,44].

3.2. Thermal Response

The maximum drill temperature (Figure 2c) ranged from 84 to 123 °C and was practically independent of drill type (107.1–107.4 °C; $p = 0.99$), but increased steadily with feed (101.5, 105.7 and 114.6 °C at 0.1, 0.2 and 0.3 mm/rev; 95% CIs 93.9–109.2, 101.5–109.9 and 110.0–119.3 °C; $p = 0.003$; 38% contribution; $\omega^2 = 0.33$) and peaked at the intermediate speed (103.0, 111.3 and 107.6 °C at 715, 1520 and 3030 rpm; $p = 0.069$; Figure S1b). The feed effect reflects the larger amount of heat generated per revolution, whereas the non-monotonic speed effect results from the competition between a higher frictional heating rate and a shorter drilling time (2.1 s at 715 rpm/0.1 mm/rev vs. 0.2 s at 3030 rpm/0.3 mm/rev), which limits conduction into the drill body; similar behaviour was reported by Ürgün et al. [20] and by Giasin and Ayvar-Soberanis [56].

The chip temperature (Figure 2d) showed the widest range (26–86 °C) and depended on the drill × speed interaction ($p = 0.018$; 45.5% contribution; $\omega^2 = 0.37$; Table 3) rather than on the main effects, in line with the chip morphology: long continuous aluminium ribbons wrapped around the drill retain heat, whereas short segmented chips cool before being imaged. The workpiece surface temperature remained low (24–43 °C, mean 30 °C), differed slightly between drills (27.2, 30.8 and 32.0 °C for HSS-R, HSS-G and carbide; $p = 0.038$) and ($r = 0.62$, 95% CI 0.31–0.81), i.e., a larger share of the ploughing energy heats the workpiece with the duller tool. No workpiece temperature approached the glass transition temperature of the epoxy matrix (120 °C for a 120 °C-curing system) or of the AF 163-2 adhesive, so thermal degradation of the interfaces can be excluded; the drill body, however, reached 112–123 °C at 0.3 mm/rev, which for HSS tools calls for lubrication or intermittent cooling at higher feeds or hole counts [57,58]. Thermograms recorded at drill withdrawal at 715 rpm (Figure S2) illustrate the local character of the temperature field around the drill, chips and workpiece; because the single-frame drill temperatures are far below the maxima of the complete records, they are used only for visualisation (Supplementary Note S1).

3.3. Entry- and Exit-Face Hole-Edge Quality

Figure 3 shows the circumferentially averaged height profiles of the entry face (upper half of each panel) and the exit face (lower half), which together form a schematic through-thickness section of the hole edge. Three trends emerge. First, the burr was always larger at the exit than at the entry face (mean burr height −3.9 µm vs. +25.7 µm; medians 2.5 and 23.0 µm; Wilcoxon signed-rank test, $p = 0.0002$, $r = 0.68$, $N = 26$, E9 excluded; Hodges–Lehmann estimate of the exit–entry difference 24.5 µm, 95% CI 13.0–45.5 µm; $p < 0.001$ with E9 included): in the 3-3/2 lay-up the breakout of the bottom 7075-T6 sheet, supported only by the thin glass/epoxy layer, determines the burr size, in agreement with the push-out mechanism [21] and with Giasin and Ayvar-Soberanis [32] and Park et al. [44]. Second, the HSS-G entry faces were the flattest ($BH_{in} = 1.6 \pm 10.2$ µm; no hole beyond ±20 µm), whereas the HSS-R and carbide drills left raised (E1, E19; E5, E11, E17, E29) or rolled-over/chipped

(E25, −75 µm; E47, −92 µm; E49 and E53, −25 µm) entry edges. Third, the carbide exit profiles peak 50–150 µm above the bottom face within 100 µm of the wall and decay over about 0.3 mm, whereas the HSS exit profiles stay within 0–40 µm.

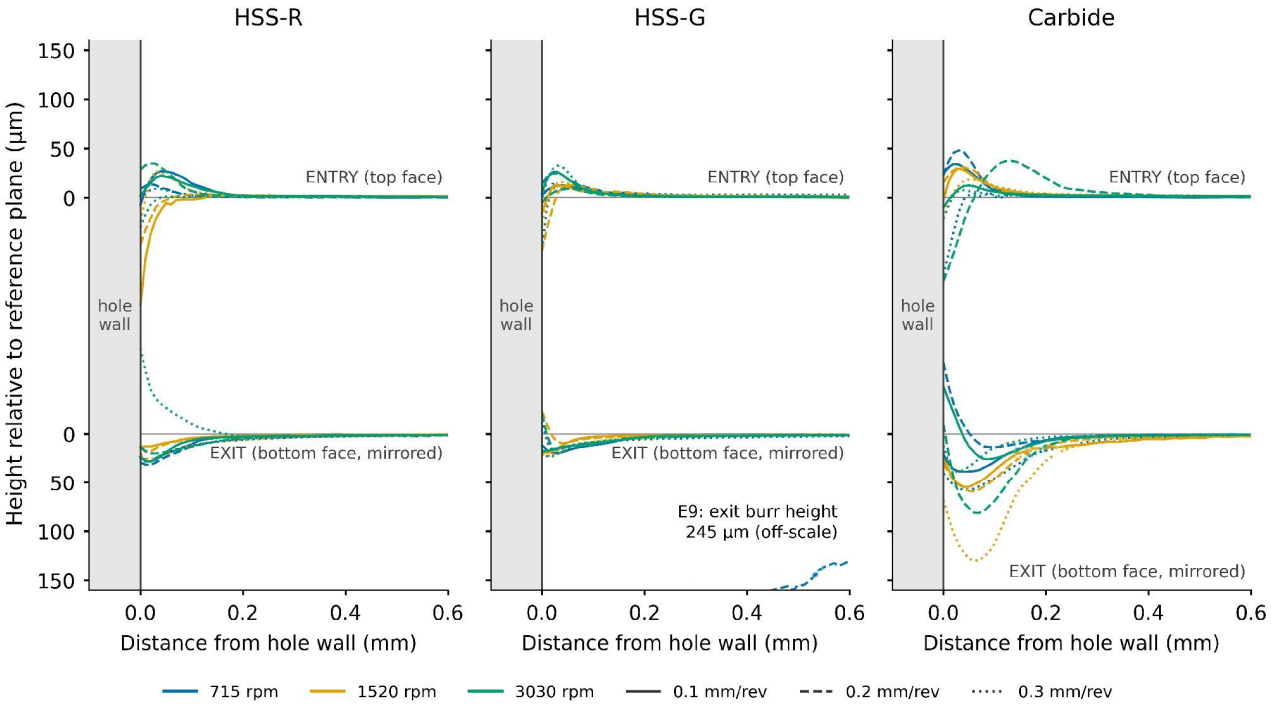


Figure 3. Circumferentially averaged hole-edge height profiles at the entry face (upper half of each panel, plotted upward) and at the exit face (lower half, mirrored downward) for the HSS-R, HSS-G and carbide drills. Profiles are aligned at the hole wall ($x = 0$) and referenced to the undisturbed sheet surface; colour denotes spindle speed, and line style denotes feed. E9 (chip clogging; dashed HSS-G curve) is shown for completeness but excluded from the group statistics (Section 2.6); its exit burr height (245 µm) lies off-scale.

Figure 4 compares the burr heights, bulging ratios and depressed fractions of the 0–300 µm edge band hole by hole. On the exit face the carbide drill produced the largest burrs (BH_{out} = 152, 91, 75 and 58 µm for E35, E23, E17 and E29; group mean 39 ± 68 µm) and the highest bulging ratio (BRout = 22.4% vs. 6.1% for HSS-R and 3.7% for HSS-G, E9 excluded; ANOVA, drill type $p = 0.003$, 57.8% contribution" ifadesi "ANOVA, drill type $p = 0.003$, 57.8% contribution, $\omega^2 = 0.53$, for which the HSS-G mean rises to 12.8%; ANOVA, drill type $p = 0.003$, 57.8% contribution, Table 3). Its exit burr was strongly parameter-dependent: the four largest burrs occurred at 1520 rpm (mean BH_{out} = 100 µm) or at 0.3 mm/rev (87 µm), whereas at 3030 rpm, BH_{out} fell to 1.5 µm on average. The carbide drill generates the largest thrust (Section 3.1), and a larger axial load on the last sheet favours plastic push-out over clean shearing [32,44]; at 3030 rpm, the higher strain rate and local temperature shear the thin sheet before it bends. The two HSS drills gave similar exit burrs (18.9 ± 17.6 µm for HSS-R and 18.4 ± 9.1 µm for HSS-G), but the ground drill was twice as repeatable and had the smallest bulging ratio. Over the 26 regular holes, the mean thrust force and BHout were uncorrelated (Pearson r = −0.11, 95% CI −0.47 to 0.29, $p = 0.61$), so tool geometry rather than force governs the burr morphology, as also found by Giasin et al. [34]; BHout and BRout were positively correlated (r = 0.68; r = 0.86 with E9 included).

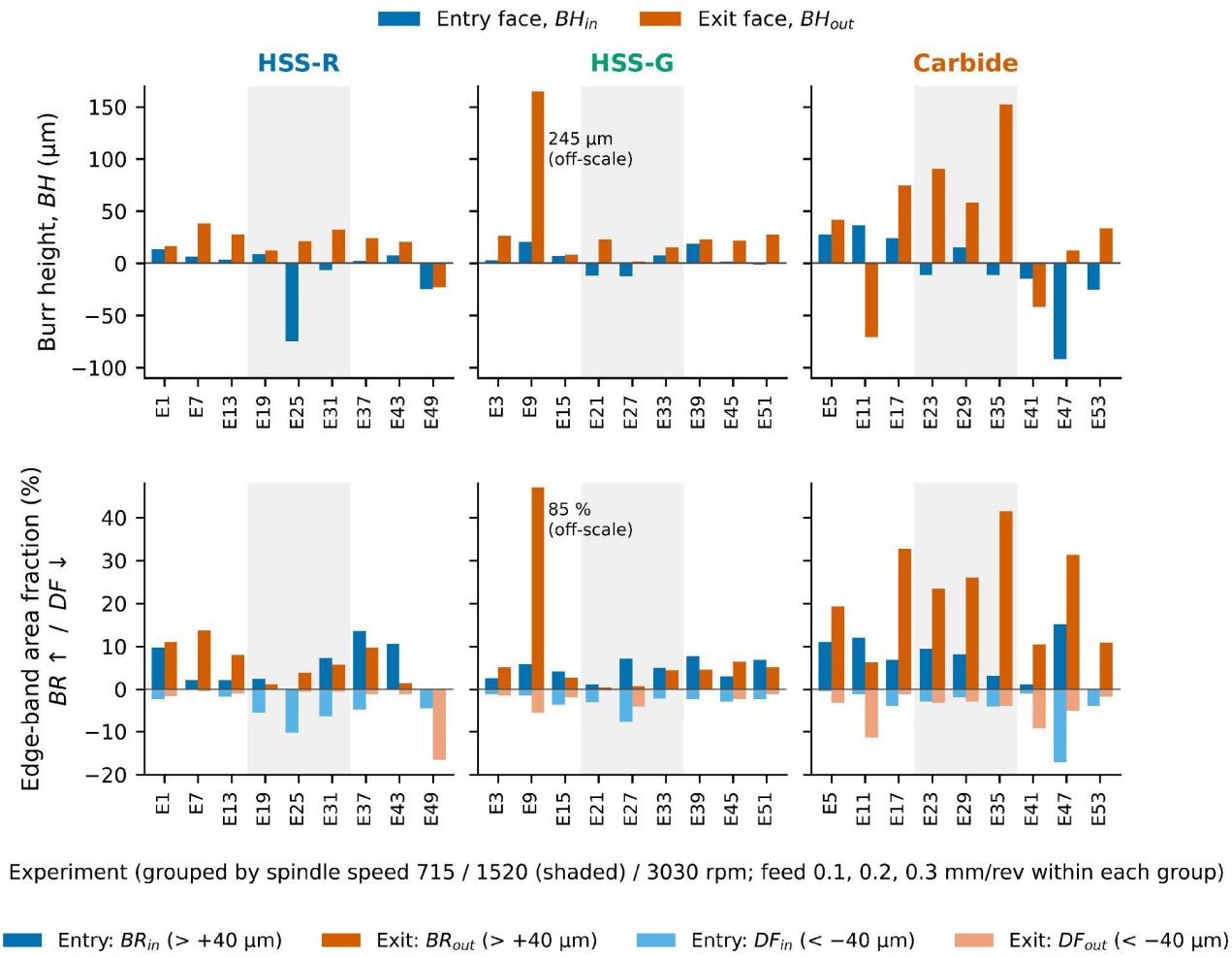


Figure 4. (**Top**) Burr height adjacent to the hole wall at the entry face (BH_{in}, blue) and at the exit face (BH_{out}, orange); positive = material protruding beyond the face; negative = edge lying inside the laminate (rounded, chipped or torn rim; Figure 1). (**Bottom**) Bulging ratio *BR* (percentage of the 0–300 µm edge band lying more than 40 µm above the reference plane, upward) and depressed fraction *DF* (more than 40 µm below, downward) at each face. Experiments are grouped by spindle speed (715/1520/3030 rpm; 1520 rpm shaded) with feed increasing from 0.1 to 0.3 mm/rev within each group; off-scale values of E9 are annotated; E9 is shown but excluded from the group statistics and tests (Section 2.6).

Since BR and DF depended on the height threshold, BR and DF were recomputed from the levelled height maps for t = 20, 30, 50, 60, and 80 µm (Table S7, Figure S10). At these heights, all conclusions at 40 µm were confirmed. The carbide drill showed the highest exit bulging ratio at each threshold (31.4% at 20 µm to 12.2% at 80 µm, compared to 13.4–0.4% for HSS-R and 12.5–0.1% for HSS-G); the drill effect was still statistically significant (Kruskal–Wallis $p = 0.0003$–0.0048), and the drill explained 49–62% of the BRout the variance in ANOVA in Table 3 ($p \leq 0.004$). The ordering of holes was preserved: the Spearman correlation with the values at 40 µm varied from 0.95 to 0.99 at thresholds 30–60 µm and dropped to 0.88 and 0.80 only at the extreme values of 20 and 80 µm. At 20 µm, the bulging ratios of the two HSS drills became close (13.4% vs. 12.5%) since, at that threshold, the band captures small but even edge undulations. On the other hand, at 80 µm, the band captures the tall carbide burrs almost exclusively (HSS drills ≤ 0.4%), and thus it could not discriminate between HSS drills anymore. There was no difference between drills at any threshold in DFin (Kruskal-Wallis $p = 0.73$–0.98), and the two holes with the maximum rounding of edges, E47 and E25, had the biggest DFin at any threshold. In the ranking of

desirability of individual holes (Table S5), the HSS-G hole drilled at 1520 rpm ranked first for all thresholds between 20 and 60 μm and ranked second at 80 μm. Consequently, the selected threshold is located inside a range over which the conclusions remain robust to its value, and at the same time it does not suffer from discrimination issues at the extremes.

Depressed and raised entry edges occurred with similar frequency (mean DFin = 3.1–4.0% for all drills); the strongest entry rounding was found for HSS-R at 1520 rpm/0.2 mm/rev (E25; DFin = 10.3%) and for carbide at 3030 rpm/0.2 mm/rev (E47; DFin = 17.1%).

The physical meaning of the sign of BH is presented in Figure 1. A positive BH entry (Figure 1b) means peel-up [21,22]: the lips and flute helix peel off the thin top sheet (0.41 mm) and the material displaced by the lip corners before the shear operation in the case of E1, E19, E5, E11, E17 and E29. A negative BH value means that the edge is below the initial surface because of one of three reasons (Figure 1c–e): (i) edge rounding caused by plastic indentation and dragging of the lip corners and margins pushing the edge material below and into the hole; (ii) chipping or tearing, when the edge material is being cut off rather than displaced; and (iii) dishing or sink-in of the thin top sheet under the thrust of the chisel edge on the underlying glass/epoxy and adhesive layer, which is much softer than 7075-T6 alloy. Three reasons differ in the radial size of the depression: dishing produces broad depression covering the whole 0–300 μm range and beyond; rounding and chipping are restricted to the area near the hole wall. In the case of E25 and E47, the depression was localised in the burr-height range (BH_{in} = −75 and −92 μm, i.e., around 20% of the sheet thickness), but the depression fraction of the 0–300 μm range was small (10.3% and 17.1%), so that the depression width would be only around 30–50 μm in the case of the full-circumference depression. Thus, these two holes are caused by edge rounding and chipping, not by dishing: in the first case, this corresponds to wandering chisel edge and unground lip corners of the rolled drill, while in the second, to high cutting speed and feed rate (606 mm/min) of the rigid carbide drill. Moderate values of E49 and E53 (−25 μm in both cases at 3030 rpm/0.3 mm/rev) mean edge rounding, while values between ±20 μm, including all HSS-G entries, correspond to sheet waviness and levelling uncertainty and can be regarded as flat edges.

Negative exit burr heights were relatively rare and were limited to the end regions of the parameter range: E11 for carbide at 715 rpm/0.2 mm/rev (−71 μm) and E41/49 for carbide/HSS-R at 3030 rpm/0.1/0.3 mm/rev (−41/−23 μm). Negative BH at the exit face suggests that the edge is situated above the original bottom surface, i.e., material removal takes place at the edge rim. There are two mechanisms which can be associated with this phenomenon (Figure 1g,h). Firstly, the final failure of the sheet in shear at the cap root prior to bending can lead to separation of the cap as a disc and leaving of the torn rim inside the sheet (Figure 1g). This case resembles the push-out burr (Figure 1f) and corresponds to the transformation of the bending-to-shear type of breakout described for drilling burrs by Kim et al. [96]. Secondly, a thin burr can be folded back into the hole under the influence of the margin during drill movement through the material (Figure 1h). In this case, the profilometer located to observe the exit face from outside will detect a rounded fold below the face instead of the protruding burr. Low bulging ratios for E41 (10.5%) and E49 (0.1%) and high strain rates at 3030 rpm make this mechanism more probable, and coincide with the shear-before-bending mechanism analysed below and in Section 3.6.1. On the contrary, in the case of E11, the highest thrust force among the series (44.0 N), combined with a low bulging ratio (6.3%), suggests that the sheet first bent outwards and then tore at the cap root, forming a recessed rim inside a slightly bulged area. In all three cases, negative BHout implies a presence of a rim defect rather than a burr-free edge; therefore, the optimisation is aimed at minimising the absolute value |BHout| rather than the signed one (Section 3.6).

The levelled height maps in Figure 5 (1520 rpm/0.1 mm/rev and the chip-clogged hole E9) illustrate these differences: the HSS-G hole is round and burr-free on both faces, the HSS-R hole is enlarged and rounded at the entry, and the carbide hole carries an asymmetric exit burr ring typical of the push-out of the last sheet when only one cutting lip carries the load. In E9, the exit sheet is bent around the whole circumference and a chip fragment adheres to the edge.

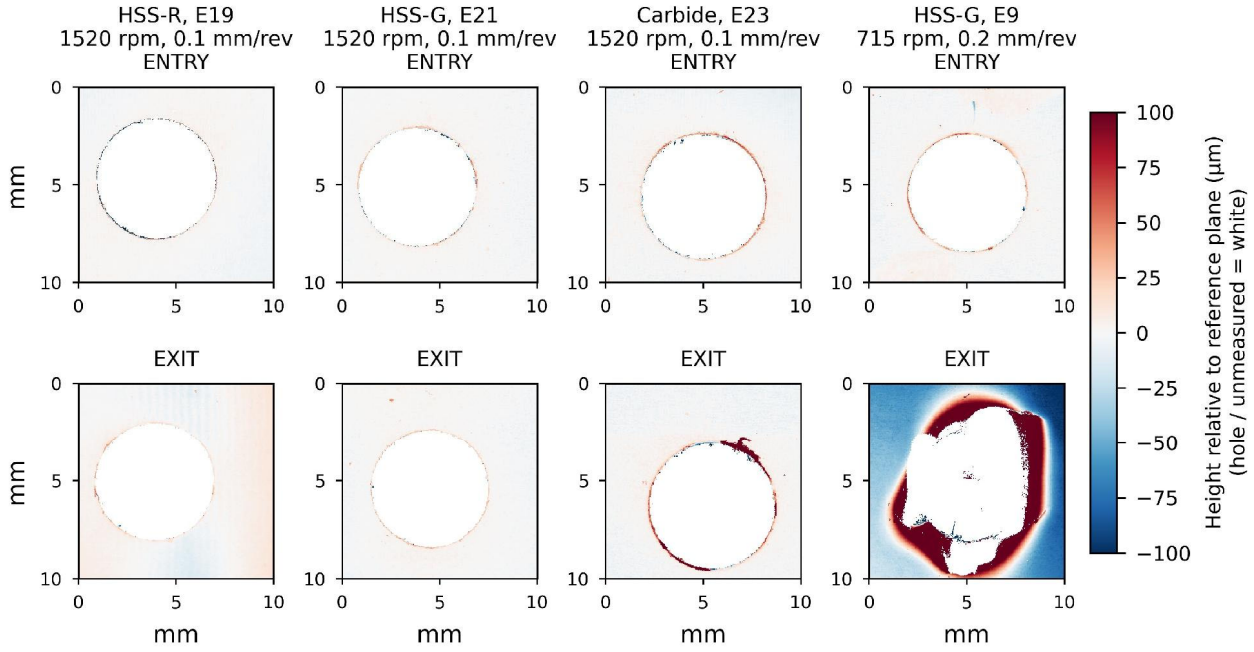


Figure 5. Levelled height maps (10 × 10 mm) of the entry (**top row**) and exit (**bottom row**) faces for the HSS-R (E19), HSS-G (E21) and carbide (E23) drills at 1520 rpm/0.1 mm/rev, and for the chip-clogged HSS-G hole E9 (715 rpm/0.2 mm/rev) shown for illustration; excluded from the face-metric statistics. Colour scale ±100 µm; white = through-hole/non-measured.

The HSS-G hole E9 (715 rpm, 0.2 mm/rev) suffered chip clogging at the drill point, which deformed the exit face severely (Figure 3, dashed curve of the HSS-G group; Figure 5): BH_{out} = 245 µm, BRout = 85%, out-of-roundness 4.0 mm and an aperture area of 38.5 mm^2 (equivalent diameter 7.0 mm instead of 5.98 mm for the other HSS-G holes). Its entry face was normal (BH_{in} = 21 µm), but its thrust force (43.6 N) and chip temperature (85 °C) were the highest of the HSS-G group. The event shows that in dry drilling of GLARE, the exit quality depends on chip evacuation as much as on the nominal parameters: continuous 7075-T6 chips can weld to the flutes of an uncoated HSS drill at low speed and turn it into a punch [12,32]. Following the rule given in Section 2.6, E9 is therefore presented in Table 2 and Figures 3–5, but not in any of the analysis involving face metric group statistics, tests, or correlations given in Sections 3.3 and 3.5. Nevertheless, its force and temperature values are still used in Sections 3.1 and 3.2. The second chip-packed hole (E45), which had a cutting speed of 3030 rpm and a feed rate of 0.2 mm/rev, resulted in an increase in the force value (41.9 N) and temperature (43.4 °C) with a regular exit face (BH_{out} = 22 µm; BRout = 6.4%). The equivalent diameter of the non-measured aperture is a threshold-free measure of the through-hole size at each face (Figure S3a), expressed as oversize relative to the nominal drill diameter (6.00 mm for HSS, 6.35 mm for carbide). The three drills differed significantly at both faces (Kruskal–Wallis; entry $p < 0.001$, $\varepsilon^2 = 0.67$; exit $p = 0.011$, $\varepsilon^2 = 0.36$; Table 4). The carbide drill gave the most accurate apertures (+25 ± 42 µm at entry, −7 ± 17 µm at exit) owing to its stiffness and precision grinding; the HSS-G drill was nearly as accurate (−8 ± 38 µm and −19 ± 40 µm, slightly undersize because of the elastic recovery of the sheets); the

HSS-R drill produced an enlarged entry aperture (+301 ± 166 µm, up to +0.48 mm) but a near-nominal exit (+38 ± 40 µm), i.e., a bell-mouthed hole caused by run-out and the poor self-centring of the unground point in thin sheets [35]. The exit out-of-roundness (Figure S3b) was similar for the three drills (394–450 µm), showed no systematic dependence on speed or feed and was governed by local burrs and chip fragments at the boundary. The instrument-reported 'Hole' and 'Peak' areas did not discriminate between the entry and exit faces (Wilcoxon test, $p = 0.22$ and 0.24) because they rely on a scan-relative height threshold (Figure S4; Supplementary Note S2).

Table 4. Hole-edge quality metrics per drill and face (mean ± sample standard deviation over the nine holes of each drill; eight for HSS-G, E9 excluded according to Section 2.6). Oversize = $D_{eq} - D_{nom}$, with D_{nom} = 6.00 mm (HSS) and 6.35 mm (carbide); *BH*: burr height; *BR*: bulging ratio; *DF*: depressed fraction.

Drill	Face	Oversize (µm)	*BH* (µm)	*BR* (%)	*DF* (%)	$D_{max} - D_{min}$ (µm)	Reported Hole Area (mm²)	Reported Peak Area (mm²)
HSS-R	Entry	+301 ± 166 (370 [160, 410])	−7.0 ± 27.7 (4 [−6, 7])	5.4 5.4 (2.6 [2.1, 9.9])	3.9	407	17.9	2.43
HSS-R	Exit	+38 ± 40 (40 [20, 50])	18.9 ± 17.6 (21 [17, 28])	6.1 (5.8 [1.4, 9.8])	2.6	450	14.8	2.40
HSS-G	Entry	−8 ± 38 (10 [−43, 20])	1.6 ± 10.2 (2 [−4, 7])	4.7 (4.7 [3.0, 7.0])	3.1	387	15.9	2.36
HSS-G	Exit	−19 ± 40 (−5 [−23, 0])	18.4 ± 9.1 (23 [14, 24])	3.7 (4.5 [2.2, 5.1])	1.4	394	13.4	2.92
Carbide	Entry	+25 ± 42 (40 [10, 50])	−5.6 ± 39.2 (−11 [−15, 24])	7.5 (8.3 [3.3, 11.1])	4.0	406	18.6	3.01
Carbide	Exit	−7 ± 17 (0 [−10, 0])	39.1 ± 67.5 (42 [12, 75])	22.4 (23.4 [10.8, 31.4])	4.6	430	19.1	1.66

3.4. Hole-Wall Morphology

Figure 6 presents the BES overviews of the twelve sectioned holes (rows: drill and feed; columns: speed). The five-layer structure (three bright 7075-T6 sheets and two glass/epoxy layers, each consisting of a light grey fabric ply between two dark, epoxy-rich adhesive layers) is resolved in every image, and the 20–60 µm dark round features in the adhesive layers are pores of the AF 163-2 film revealed by sectioning, not drilling damage. The two drills produced clearly different walls. The HSS-R holes (Figure 6a–f) show irregular, fibre-covered glass/epoxy layers, ragged top-sheet edges at 1520 rpm/0.1 mm/rev and 715 rpm/0.3 mm/rev (Figure 6b,d), a lifted chip fragment at 3030 rpm/0.1 mm/rev (Figure 6c), a burr lip at 1520 rpm/0.3 mm/rev (Figure 6e) and local tearing and smearing of the middle sheet at 3030 rpm/0.3 mm/rev (Figure 6f). The carbide holes (Figure 6g–l) show uniform, continuous layers with straight sheet/composite boundaries; the only macroscopic defects are loose fibre fragments at 715 rpm/0.3 mm/rev (Figure 6j) and, at 1520 rpm/0.3 mm/rev (Figure 6k), two zones where the top sheet bent away from the composite and debonded from the adhesive over several hundred micrometres. This is the hole with the largest exit burr of the series (E35; BH_{out} = 152 µm, BRout = 41.5%): the last sheet was pushed out by the chisel edge and bent before being sheared, as described by the push-out model of Hocheng and Dharan [21].

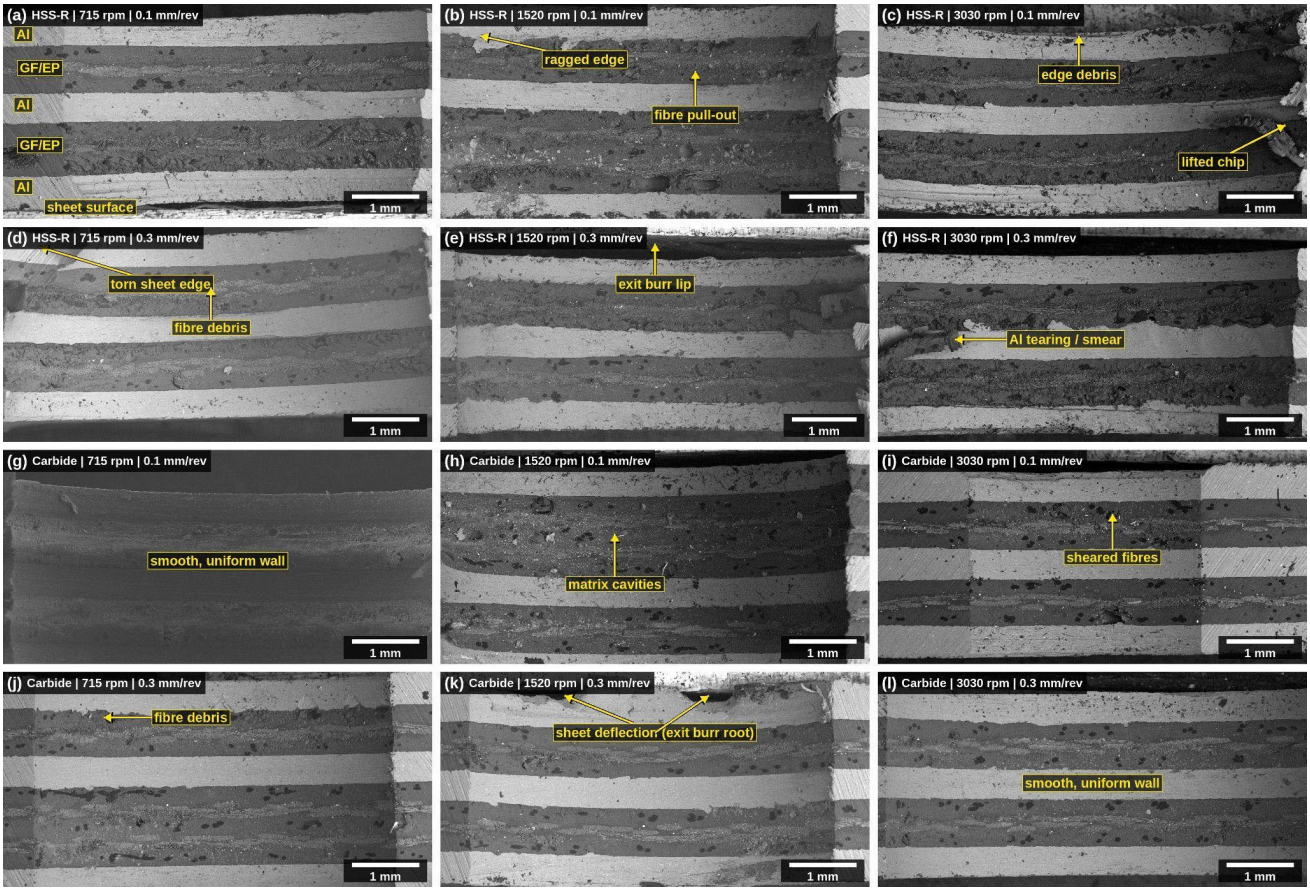


Figure 6. Backscattered-electron SEM images (×20) of the sectioned hole walls for the HSS-R drill (**a**–**f**) and the carbide-tipped drill (**g**–**l**) at 715, 1520 and 3030 rpm (columns) and feeds of 0.1 and 0.3 mm/rev (rows); (**g**) was recorded in secondary-electron mode. Bright bands: 7075-T6 sheets; grey bands: glass/epoxy layers with the fabric ply in their centre. The face at the top of each panel is the exit sheet surface. Arrows mark the macroscopic wall defects discussed in the text. Scale bars: 1 mm.

At ×100 (Figure 7), the HSS-R walls display circumferential feed marks on the aluminium (Figure 7a), a ploughed and torn surface with adhering debris at 1520 rpm/0.1 mm/rev (Figure 7c) and aluminium smeared over the adjacent adhesive at 3030 rpm/0.3 mm/rev (Figure 7f). The fibres are not cut cleanly: bundles parallel to the wall are pulled out (Figure 7a,d,e), transverse bundles are crushed into fragments lying on the wall (Figure 7a–c,e), and the matrix between them is smeared or stripped. In the adhesive interlayers, the resin is torn out in chunks at 1520 rpm (Figure 7c,d), an aluminium chip fragment is welded to the wall at 715 rpm/0.3 mm/rev (Figure 7b), and at 3030 rpm/0.3 mm/rev, the adhesive peels away from the middle sheet over more than 0.5 mm (interfacial debonding, Figure 7f). These features are typical of an edge that bends and breaks the fibres instead of shearing them: the rolled drill has an unground, rounded edge and a thick web, as reported for blunt or worn tools in FRP drilling and trimming [15,16,88]. Increasing the feed from 0.1 to 0.3 mm/rev shifts the damage from the plies to the interfaces (matrix chipping, aluminium smearing and debonding), consistent with the higher chip load per lip and the higher drill temperature at 0.3 mm/rev (Section 3.2), whereas increasing the speed did not clean the HSS-R wall, in contrast to its effect on the exit burr (Section 3.3).

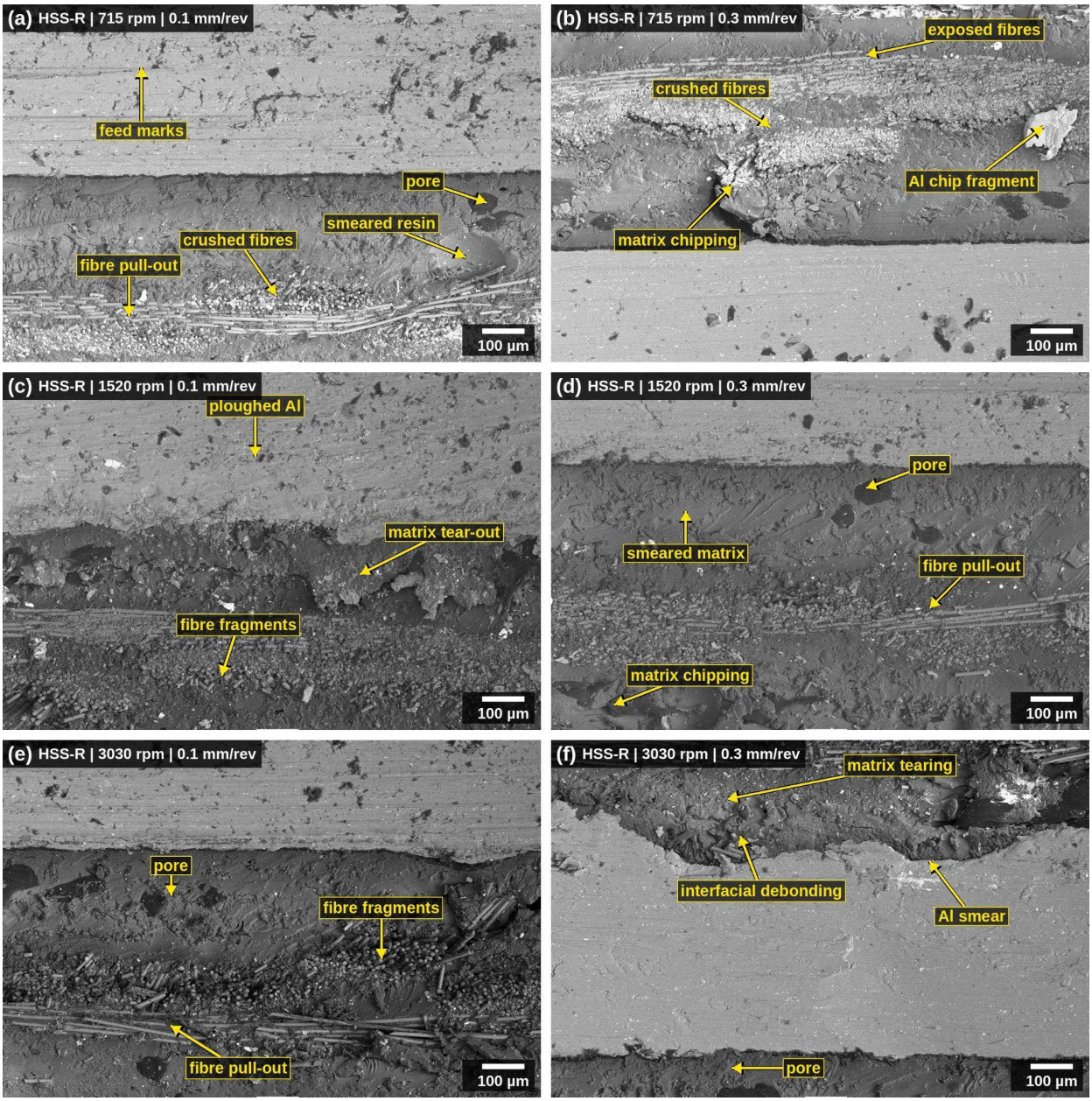


Figure 7. Backscattered-electron SEM images (×100) of the hole walls drilled with the rolled HSS drill at (**a**) 715 rpm/0.1 mm/rev (E1), (**b**) 715 rpm/0.3 mm/rev (E13), (**c**) 1520 rpm/0.1 mm/rev (E19), (**d**) 1520 rpm/0.3 mm/rev (E31), (**e**) 3030 rpm/0.1 mm/rev (E37) and (**f**) 3030 rpm/0.3 mm/rev (E49). Arrows mark feed marks and ploughing of the aluminium sheets, fibre pull-out, crushed fibres and fibre fragments in the glass-fabric plies, smeared, chipped or torn-out matrix in the adhesive interlayers, pores of the adhesive film, an adhered aluminium chip fragment and interfacial debonding. Scale bars: 100 µm.

The carbide walls (Figure 8) show a cutting-dominated process: small regular feed marks without ploughing (Figure 8a,e,f), clean and straight sheet/composite boundaries (Figure 8a), transversely sheared fibre ends flush with the wall (Figure 8a,c,e,f) and a thin glossy film of smeared resin partly covering them (Figure 8a,d), with few loose particles. Three departures are informative. At 715 rpm/0.3 mm/rev (Figure 8b), the lowest cutting speed (14.3 m/min) combined with the highest chip load, the aluminium at the sheet boundary is smeared and flaked over the adjacent layer and the adhesive is flaked. At 1520 rpm/0.3 mm/rev (Figure 8d), the fabric ply is broken into fine fragments, the smeared

matrix is cracked, and the composite layer protrudes above the aluminium (interface step), indicating softening and displacement of the adhesive. At 3030 rpm and 0.1 or 0.3 mm/rev (Figure 8e,f), a chipped adhesive fragment and a bright aluminium film smeared over the composite are seen. Aluminium particles and smears on the composite wall (Figure 8c,f) originate from chips carried by the flutes into the softer layers, as is typical of dry one-shot drilling of metal–composite stacks [12,87].

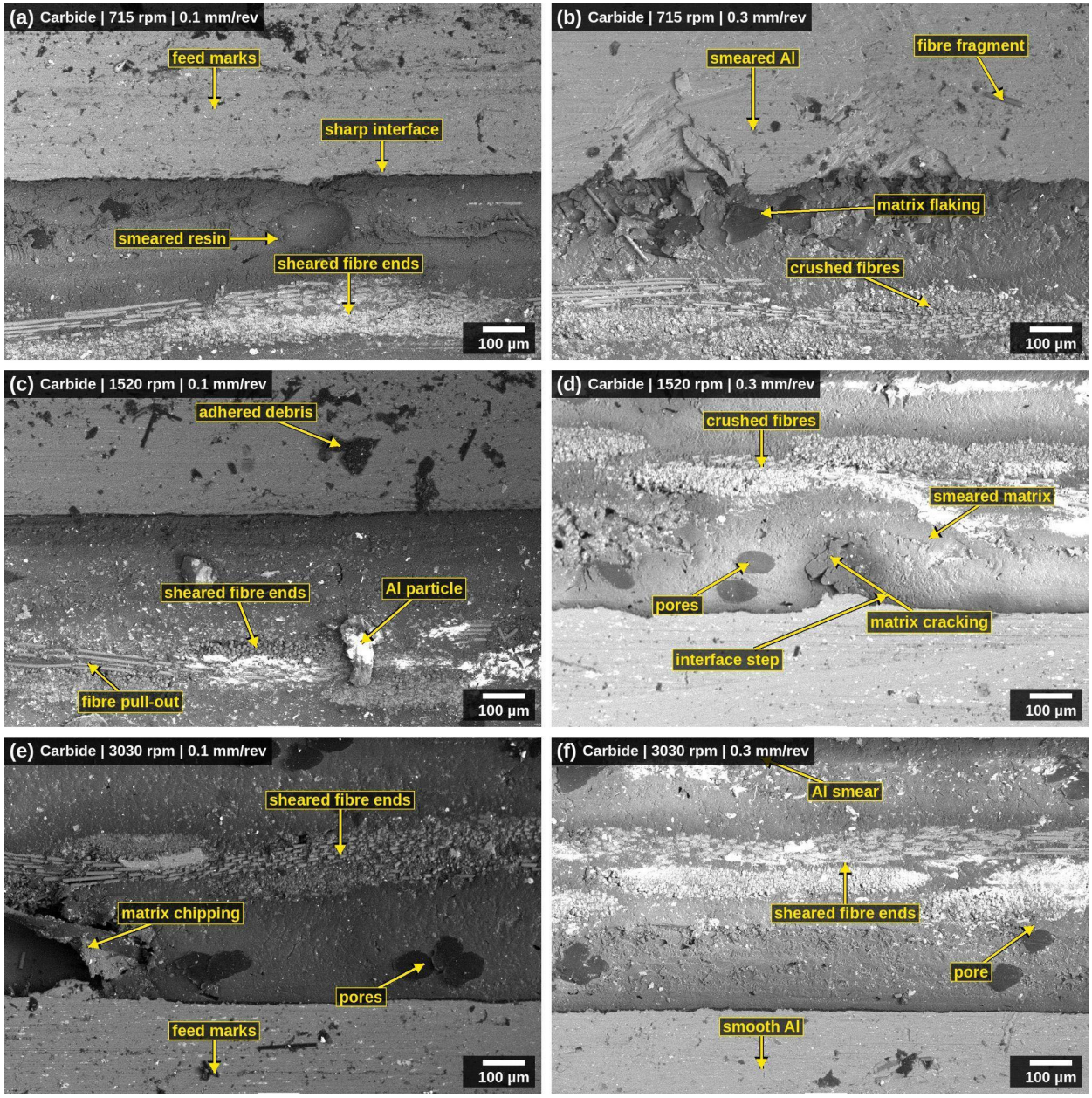


Figure 8. Backscattered-electron SEM images (×100) of the hole walls drilled with the carbide-tipped drill at (**a**) 715 rpm/0.1 mm/rev (E5), (**b**) 715 rpm/0.3 mm/rev (E17), (**c**) 1520 rpm/0.1 mm/rev (E23), (**d**) 1520 rpm/0.3 mm/rev (E35), (**e**) 3030 rpm/0.1 mm/rev (E41) and (**f**) 3030 rpm/0.3 mm/rev (E53). Arrows mark the regular feed marks and the sharp sheet/composite interface, transversely sheared fibre ends, smeared resin, smeared or flaked aluminium, matrix flaking and cracking, crushed fibres, adhered debris and aluminium particles, the interface step and pores of the adhesive film. Scale bars: 100 µm.

The SEM observations complement the profilometry in three respects. First, the ranking of the two drills reverses between the hole faces and the hole wall: the carbide drill, which

produced the largest exit burrs and bulging ratios (Section 3.3), gave the cleanest walls, whereas the rolled HSS drill, whose exit burr never exceeded 40 µm, produced fibre pull-out, matrix chipping and interfacial debonding. The exit burr is a plastic-bending defect controlled by the axial load and the drill rigidity, whereas wall damage is a cutting defect controlled by edge sharpness; a sharp, stiff carbide edge reduces the latter and increases the former, in agreement with Giasin et al. [34] and Park et al. [44]. Second, the glossy matrix and the cracked or displaced adhesive at 0.3 mm/rev reflect the drill temperatures of 112–123 °C at that feed (Section 3.2), close to the glass transition of a 120 °C-cured epoxy: although the bulk workpiece does not exceed 43.4 °C, the wall is heated locally by the tool margin, as discussed by Merino-Pérez et al. [58,59] for CFRP. Third, the aluminium fragments welded to or smeared over the composite (Figures 7b and 8c,f) and the lifted chip fragment at 3030 rpm (Figure 6c) are the wall counterpart of the chip-evacuation problem observed at the exit face, as reported for GLARE [32] and FRP/aluminium stacks [12], and support the use of peck drilling or through-tool air at these feeds. Together with the flat entry edges and accurate apertures in Section 3.3, the SEM results show that a sharp, symmetrically ground cutting edge is the primary requirement for damage-free dry drilling of thin GLARE. The SEM study was qualitative, covered twelve of the 27 holes and did not include the HSS-G drill, so the wall morphology at the optimum condition in Section 3.6 (HSS-G, 1520 rpm, 0.2 mm/rev) remains to be verified.

3.5. Relations Between Force, Temperature and Edge Quality

Neither the mean thrust force nor the maximum drill temperature predicts the exit burr across drill types (Figure S5): the largest burrs were produced at thrust forces (36.8–40.7 N) and drill temperatures (107–120 °C) at which the HSS holes were burr-free. E9 is shown in Figure S5 but excluded from the correlations (Section 2.6). Within the HSS-R group, however, BH_{out} decreased with increasing thrust force (Spearman $\rho = -0.69$, bootstrap 95% CI −0.98 to −0.02, $p = 0.038$), i.e., the most aggressive cut at 3030 rpm gave the best exit edge because the last sheet was sheared rather than bent; this relation rests on nine holes and should be regarded as indicative. Table 4 summarises the edge-quality metrics per drill and face.

3.6. Contribution Analysis and Multi-Objective Optimisation

The ANOVA in Table 3 used the unreplicated first series. The complete data set comprises three replicated series of the 3^3 plan (81 measurements), which allows the full model, including the three-factor interaction, to be estimated with 54 error degrees of freedom. This section ranks the effects of drill type, speed and feed on five hole-quality criteria and then finds the best compromise among the 27 measured conditions with a weighted desirability function [64] and exhaustive grid search; RSM [62,63] is used to describe the response trends and, for exploration only, to search a refined grid; previous multi-criteria studies of FML drilling relied mainly on Taguchi-based grey relational analysis [46,51] and on RSM with ANOVA [54]. The five responses are F_{max}, T_w, T_{max}, BH_{out} and BRout (Section 2.4). BH_{out} is a non-contact, circumferentially averaged counterpart of the stylus-measured burr heights reported for GLARE and metals [32,34,66,96], so absolute values should not be compared directly with the literature; BRout, introduced here, quantifies the circumferential extent of the push-out of the bottom sheet. Because depressed edges are also defects (rounded, chipped or torn rims; Section 3.3, Figure 1), $|BH_{out}|$ is minimised in the optimisation, whereas the signed BH_{out} is used in the contribution analysis (negative condition means occurred for carbide at 715 rpm/0.2 mm/rev and 3030 rpm/0.1 mm/rev and for HSS-R at 3030 rpm/0.3 mm/rev). Unlike the case of hole-by-hole consideration, the chip-clogged situation (HSS-G, 715 rpm, 0.2 mm/rev) is retained in this region because,

as seen in Section 2.6, the optimisation is against those process conditions susceptible to failure; this effect on the contribution is measured in Section 3.6.1.

3.6.1. Contribution Analysis

The contribution of each term is its sum of squares as a percentage of the total over the 81 observations (Table 5; Figure S6). The full model explained 97.8–99.98% of the variation in the five responses and the replicate error explained only 0.02–2.24%. Because the error mean square is so small, almost every term is statistically significant, so the terms are ranked by their contributions. This small error should not be regarded as a sign of a very reproducible drilling process because replicates were performed inside the batch, and the error term is primarily due to repeatability of the measurement process. A less optimistic reference value is the 27-holes ANOVA given in Table 3, where the pooled three-factor interaction term, which accounts for 14–21% of the variance, plays the role of the error term. The most important effects indicated in Table 5 correspond to the leading terms of this analysis and make a similar contribution: type of the drill for the thrust force (51.9% vs. 29.6% for the average thrust force), feed rate for the maximum temperature of the drill (45.6% vs. 38.0%), and type of the drill for the exit bulging ratio after compensating for the chip-clogged hole (57.0% vs. 57.8%). Thus, the relative importance of these effects does not depend on the size of the error of replication. On the other hand, the individual terms of two- and three-factor interactions for the edge responses can be separated from hole-to-hole variance using the present data set only qualitatively.

Table 5. Percentage contributions of drill type, spindle speed, feed and their interactions to the variation of the responses (full 3^3 factorial model, three replicates, 81 observations; d.f. = degrees of freedom; signed BH_{out}). The chip-clogged condition (HSS-G, 715 rpm, 0.2 mm/rev) is included; the contributions obtained when its observations are replaced by the mean of the remaining conditions are given in Section 3.6.1.

Source	d.f.	F_{max} (N)	T_w (°C)	T_{max} (°C)	BH_{out} (µm)	BR_{out} (%)
Model	26	97.76	99.66	98.69	99.98	99.97
Linear	6	58.77	46.16	57.56	12.76	28.11
Drill type	2	51.92	35.88	2.59	3.46	14.82
Spindle speed	2	5.45	6.73	9.42	7.89	7.72
Feed	2	1.40	3.55	45.55	1.41	5.57
Two-way interactions	12	19.21	27.84	26.87	52.93	36.83
Drill × Speed	4	9.07	8.91	6.84	24.94	14.55
Drill × Feed	4	5.20	9.00	6.80	23.12	13.89
Speed × Feed	4	4.94	9.93	13.23	4.87	8.39
Three-way interaction	8	19.77	25.66	14.26	34.29	35.02
Drill × Speed × Feed	8	19.77	25.66	14.26	34.29	35.02
Error	54	2.24	0.34	1.31	0.02	0.03
Total	80	100.00	100.00	100.00	100.00	100.00

Drill type dominated the thermo-mechanical responses. It contributed 51.9% to F_{max} (speed 5.5%, feed 1.4%), with means of 33.8 N for HSS-G, 38.6 N for HSS-R and 41.8 N for the carbide drill, confirming the ranking of the 27-hole ANOVA. The order follows the chisel-edge geometry that carries most of the axial load: the carbide drill is 6% larger in diameter and less sharp, so a larger share of its thrust goes into ploughing, whereas the sharp, symmetrically ground lips and thin web of the HSS-G drill shear the 7075-T6 sheets and the glass/epoxy plies. Feed is unimportant because the chip thickness per lip ($f/2$ = 0.05–0.15 mm) is limited and the chisel edge engages one 0.41 mm sheet at a time; the 19.8% three-factor interaction reflects the chip-packing events of the HSS-G drill at 0.2 mm/rev (E9, E45; F_{max} = 38.0 N vs. 32.5 N in the other HSS-G conditions). Drill type also governed T_w (35.9%; 31.0, 28.8 and 27.0 °C for carbide, HSS-G and HSS-R), consistent with

the correlation between T_w and thrust (r = 0.62), whereas speed (6.7%) and feed (3.6%) mattered little because of the short contact time (0.2–2.1 s); the isolated warm conditions behind the 25.7% three-factor term (33.8–35.4 °C) all remained far below the glass transition of the epoxy. Feed was the leading predictor of T_{max} (45.6%; 102.3, 105.8 and 116.2 °C at 0.1, 0.2 and 0.3 mm/rev), speed acted non-monotonically (9.4%; 104.3, 110.2 and 109.7 °C at 715, 1520 and 3030 rpm) through the competition between heat generation and drilling time, which also explains the 13.2% speed × feed interaction, and drill type was minor (2.6%; 107.8, 106.5 and 109.9 °C for HSS-R, HSS-G and carbide).

The edge responses behaved differently: the main effects explained only 12.8% of the variance of BH_{out}, the two-factor interactions 52.9% (drill × speed 24.9%, drill × feed 23.1%) and the three-factor interaction 34.3%. Burr height therefore cannot be controlled by speed or feed alone; their effect depends on the drill. For the carbide drill the mean BH_{out} was 14.5, 98.6 and 1.8 µm at 715, 1520 and 3030 rpm and 30.2, −0.8 and 85.5 µm at 0.1, 0.2 and 0.3 mm/rev, whereas the HSS drills stayed within 7–27 µm (HSS-R) and 12–24 µm (HSS-G, excluding the chip-clogged condition) at all settings. The exit burr forms when the unsupported bottom sheet is displaced by the chisel edge and then sheared by the lips [21], and its type and size depend on the cutting conditions and the drill geometry [96]: if the axial load and strain rate cause shear failure, the burr is small, whereas if the sheet yields under the lips, a tall burr or a rolled edge results. The large-diameter carbide drill transfers the highest axial load through its chisel edge and displaces the sheet at 1520 rpm or 0.3 mm/rev, whereas at 3030 rpm the sheet is sheared before it can bend (Section 3.3); the smaller load and sharper lips of the HSS drills give a flat response. The bulging ratio followed the same pattern (main effects 28.1%, two-factor interactions 36.8%, three-factor interaction 35.0%), and the three-factor term is dominated by a single condition: the chip-clogged HSS-G condition at 715 rpm/0.2 mm/rev (condition means BH_{out} = 239 µm, BRout = 83%) accounts for 49.8% and 59.9% of the total sums of squares of BH_{out} and BRout. Replacing its three observations with the mean of the remaining conditions raised the drill-type contribution to BRout from 14.8% to 57.0% (57.8% in Table 3, where E9 was removed), reduced the three-factor term to 17.3% (BRout) and 16.6% (BH_{out}) and raised the drill × speed term for BH_{out} to 29.3%. Without the chip-clogged condition, the carbide drill retains the highest bulging ratio (22.3% vs. 6.1% for HSS-R and 3.7% for HSS-G), consistent with its larger axial load and the push-out mechanism, and the weight of this single condition confirms that chip evacuation can outweigh the nominal parameters.

3.6.2. Problem Formulation and Response-Surface Models

The decision variables are the drill type (HSS-R, HSS-G, carbide), the spindle speed n (715–3030 rpm, i.e., 13.5–57.1 m/min for the Ø6.00 mm drills and 14.3–60.4 m/min for the Ø6.35 mm carbide drill) and the feed f (0.10–0.30 mm/rev). Five responses are minimised simultaneously: F_{max}, T_w, T_{max}, $|BH_{out}|$ and BRout. Importance weights of 3 were assigned to the three thermo-mechanical responses and 5 to the two edge responses (Table 6), because the exit burr is the dominant defect of the 3-3/2 laminate (Section 3.3) and requires secondary removal. Each response yi was converted into a one-sided smaller-is-better desirability di [64] with the lower and upper limits Li and Ui equal to the minimum and maximum of the 81 measurements (Equation (6)), and the responses were combined into the weighted composite desirability D (Equation (7)):

$$d_i = 1\ (y_i \le L_i);\ d_i = [(U_i - y_i)/(U_i - L_i)]^s\ (L_i < y_i < U_i);\ d_i = 0\ (y_i \ge U_i);\ s = 1 \quad (6)$$

$$D = (d_1{}^3 \cdot d_2{}^3 \cdot d_3{}^3 \cdot d_4{}^5 \cdot d_5{}^5)^{1/19} \quad (7)$$

where d1…d5 refer to F_{max}, T_w, T_{max}, $|BH_{out}|$ and BR_{out} and the exponents are the weights (Σwi = 19). Because the geometric mean is zero when any response reaches its upper

limit, a condition cannot score well by excelling in four responses while failing in the fifth. The weighted-sum score S [99] was computed as an independent cross-check (Equation (8)). The problem is to maximise D(drill, n, f) subject to 715 ≤ n ≤ 3030 rpm and 0.10 ≤ f ≤ 0.30 mm/rev.

$$S = (3d_1 + 3d_2 + 3d_3 + 5d_4 + 5d_5)/19 \quad (8)$$

Table 6. Optimisation objectives, importance weights and desirability limits (L_(i), U_(i) = minimum and maximum of the 81 observations). U_(i) of |BH_(out)| and BR_(out) is set by the chip-clogged condition (HSS-G, 715 rpm, 0.2 mm/rev). The effect of these limits on the optimum is examined in Section 3.6.5 (Table 9).

Response	Symbol	Goal	Weight	Normalised Weight	L_i	U_i
Maximum thrust force (N)	F_{max}	Minimise	3	0.158	29.6	46.6
Workpiece temperature (°C)	T_w	Minimise	3	0.158	24.7	35.55
Maximum drill temperature (°C)	T_{max}	Minimise	3	0.158	84.3	128.2
Exit burr height, magnitude (µm)	$\|BH_{out}\|$	Minimise	5	0.263	1.8	239.5
Exit bulging ratio (%)	BR_{out}	Minimise	5	0.263	0.1	83.3

Because drill type is categorical, drill-wise second-order models (six coefficients from nine conditions per drill) were considered first, but leave-one-condition-out cross-validation, in which the three replicates of one condition are removed in turn, gave negative cross-validated R^2 for all five responses (−0.62 to −3.87), and they were discarded. The continuous variables were therefore coded according to Equation (9), with a logarithmic speed coding that places the step-pulley speeds 715, 1520 and 3030 rpm at $x_1 = -1$, +0.04 and +1, and pooled second-order models with drill-specific intercepts were fitted (Equation (10)):

$$x_1 = [\ln n - 1/2(\ln 715 + \ln 3030)]/[1/2 \ln(3030/715)], x_2 = (f - 0.20)/0.10 \quad (9)$$

$$y = \beta_0 + \beta_G D_G + \beta_C D_C + \beta_1 x_1 + \beta_2 x_2 + \beta_{11} {x_1}^2 + \beta_{22} {x_2}^2 + \beta_{12} x_1 x_2 + \varepsilon \quad (10)$$

where DG and DC are indicator variables for the HSS-G and carbide drills (HSS-R is the reference level). The models were fitted by ordinary least squares to all 81 observations (8 coefficients, 73 residual degrees of freedom) with a lack-of-fit test based on the pure error of the replicates. Two grids were searched exhaustively: Grid A, the 27 machine-feasible conditions, evaluated with the measured condition means from three replicates, and Grid B, a refined grid of 3 drills × 464 speeds (715–3030 rpm, 5 rpm step) × 41 feeds (0.100–0.300 mm/rev, 0.005 mm/rev step), i.e., 57,072 RSM predictions with the edge responses clamped at zero. The complete set of control parameters and the workflow are given in Table S2 and Figure S7.

3.6.3. Response-Surface Results

The pooled models describe the thermo-mechanical responses reasonably well (adjusted R^2 = 0.57 for F_{max}, 0.41 for T_w and 0.66 for T_{max}; cross-validated R^2 = 0.20, −0.07 and 0.37), whereas the edge-quality models explain only 16–22% of the variance and have negative cross-validated R^2 (−0.45 and −0.34); the lack-of-fit test was significant for all responses ($p < 0.001$) because the pure error of the replicates is extremely small (median coefficient of variation (CV) 2.0% for F_{max} and 2.8% for BH_{out}). First-order models gave slightly higher cross-validated R^2 for F_{max} and T_w (0.28 and 0.13), but a lower value for T_{max} (0.25 vs. 0.37), so the second-order form was retained; the full statistics are listed in Table S3. The coefficients (Table 7) confirm the contribution analysis: the carbide drill raises F_{max} by 3.2 N and T_w by 4.0 °C, HSS-G lowers F_{max} by 4.8 N relative to HSS-R ($p < 0.001$), the positive curvature of F_{max} in speed (β11 = 2.20 N, $p <$ 0.01) places its minimum at 1390 rpm, where the main-effect plot shows a shallow minimum,

and T_{max} depends on feed (β2 = 6.98 °C) and on the speed × feed interaction (β12 = −4.38 °C; both $p < 0.001$), which corresponds to the trade-off between heat input and drilling time. For the edge responses, only the carbide intercept (+39.7 µm and +16.2%) and the negative linear speed term (−17.6 µm and −5.7% per coded unit) are significant, i.e., a higher speed reduces both burr height and bulging ratio, as in RSM studies of drilling burrs in aluminium-matrix composites [65,66]. Because their cross-validated R^2 is negative, the edge-quality models have no predictive value between the measured conditions. They are therefore used only to indicate the direction of the speed effect (Table 7) and not to select the recommended condition.

Table 7. Coded regression coefficients of Equation (10) (* $p < 0.05$, ** $p < 0.01$, *** $p < 0.001$).

Response	β_0	β_G	β_C	β_1	β_2	β_{11}	β_{22}	β_{12}
F_{max} (N)	37.81 ***	−4.79 ***	3.20 ***	0.35	0.17	2.20 **	−1.10	1.03 *
T_w (°C)	26.80 ***	1.79 **	4.02 ***	0.69 *	0.48	0.96	−0.70	0.08
T_{max} (°C)	107.53 ***	−1.34	2.06	2.72 ***	6.98 ***	−3.05 *	3.46 **	−4.38 ***
$\lvert BH_{out}\rvert$ (µm)	36.39 **	19.02	39.70 **	−17.56 **	5.17	−2.60	−15.71	−2.10
BR_{out} (%)	9.99 *	6.48	16.19 ***	−5.66 **	1.40	2.55	−8.32 *	−1.21

The response surfaces and the measured condition means are shown in Figure 9. By construction, the three drill surfaces are parallel and differ only in their intercepts (Table 7). The measured means scatter widely around the smooth edge-response surfaces (Figure 9d,e), most strongly at the isolated conditions with burr heights above 140 µm, in line with the low R^2 values: edge-defect formation is governed by condition-specific events rather than by a smooth function of speed and feed. The composite-desirability surfaces (Figure 9f; refined grid in Figure S8) peak at low feed and intermediate speed and are lower for the carbide drill than for the HSS drills.

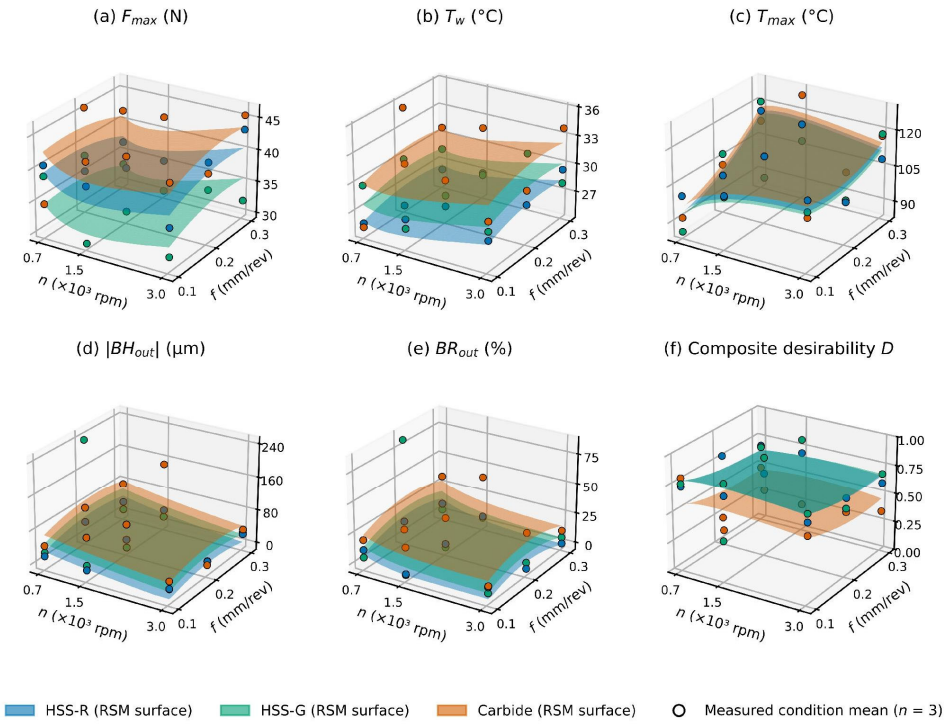


Figure 9. RSM surfaces of (**a**) F_{max}, (**b**) T_w, (**c**) T_{max}, (**d**) $|BH_{out}|$, (**e**) BR_{out} and (**f**) composite desirability D as functions of spindle speed and feed for the three drills (pooled second-order models, Equation (5)); circles are the measured condition means of three replicates; predictions of the edge responses are clamped at zero. The chip-clogged condition is included in the fits and in the plotted means.

3.6.4. Optimum Conditions

On the machine-feasible grid (Table 8; complete ranking in Table S1 and Figure S9) the highest desirability, D = 0.867, was obtained for the HSS-G drill at 1520 rpm and 0.2 mm/rev (F_{max} = 31.1 N, T_w = 27.2 °C, T_{max} = 102.5 °C, $|BH_{out}|$ = 1.8 µm, BRout = 0.8%), followed by HSS-G at 1520 rpm with 0.1 mm/rev (D = 0.852) and 0.3 mm/rev (D = 0.825). The three best conditions thus form a plateau of the ground HSS drill at the intermediate speed, irrespective of feed. The best condition has almost perfect edge desirabilities (1.00 and 0.99) but the lowest desirability of its five components for the drill temperature (0.59). Ranks four and five (carbide at 715 rpm/0.1 mm/rev and HSS-R at 715 rpm/0.2 mm/rev) combine low drill and workpiece temperatures (91.8 and 98.9 °C; 25.4 and 24.9 °C) with higher thrust (34.6 and 35.8 N) and sizeable burrs ($|BH_{out}|$ = 42 and 38 µm). The worst conditions are the chip-clogged HSS-G condition at 715 rpm/0.2 mm/rev (D = 0.027; $|BH_{out}|$ = 239 µm, BRout = 83%), carbide at 715 rpm/0.2 mm/rev (D = 0.241) and carbide at 1520 rpm/0.3 mm/rev (D = 0.235; T_{max} = 127.4 °C, $|BH_{out}|$ = 148 µm). The weighted-sum score gave almost the same ranking (Spearman ρ = 0.98; identical top five).

Table 8. The ten best machine-feasible conditions ranked by composite desirability *D* (measured condition means, *three replicates*). *S*: weighted-sum score (Equation (8)); RSM *D* (rank): composite desirability predicted by the RSM and its rank among the 27 conditions. The complete ranking is given in Table S1.

Rank	Drill	*n* (rpm)	*f* (mm/rev)	F_{max} (N)	T_w (°C)	T_{max} (°C)	$\|BH_{out}\|$ (µm)	BR_{out} (%)	*D*	*S*	RSM *D* (rank)
1	HSS-G	1520	0.2	31.1	27.2	102.5	1.8	0.8	0.867	0.882	0.712 (8)
2	HSS-G	1520	0.1	30.3	26.5	105.0	22.9	0.4	0.852	0.869	0.807 (2)
3	HSS-G	1520	0.3	30.4	26.7	107.9	16.0	4.6	0.825	0.848	0.682 (12)
4	Carbide	715	0.1	34.6	25.4	91.8	42.0	19.5	0.808	0.811	0.573 (20)
5	HSS-R	715	0.2	35.8	24.9	98.9	37.9	13.6	0.796	0.805	0.679 (14)
6	HSS-G	3030	0.1	31.8	28.5	108.0	22.8	4.6	0.777	0.801	0.769 (5)
7	HSS-G	715	0.1	38.9	29.8	86.0	26.2	5.0	0.758	0.790	0.784 (3)
8	HSS-R	1520	0.1	39.1	27.4	105.6	12.3	1.2	0.744	0.780	0.812 (1)
9	HSS-R	715	0.1	40.6	25.8	100.9	17.0	11.3	0.732	0.770	0.779 (4)
10	HSS-R	1520	0.2	38.0	26.0	111.4	21.2	3.8	0.731	0.773	0.718 (7)

The exploratory search of the refined RSM grid (57,072 candidates) gave its highest predicted D for the HSS-R drill at 1325 rpm and the minimum feed of 0.100 mm/rev (D = 0.814); the best HSS-G candidate (1295 rpm, 0.100 mm/rev; D = 0.809) is almost equal and the best carbide candidate much lower (1390 rpm, 0.100 mm/rev; D = 0.624). The predicted responses at the HSS-R optimum are F_{max} = 36.7 ± 1.8 N, T_w = 25.5 ± 1.2 °C, T_{max} = 102.9 ± 3.0 °C, $|BH_{out}|$ = 17.7 ± 26.3 µm and BRout = 1.0 ± 9.0% (95% confidence intervals of the mean; Table S4). The two optimisations agree on the HSS drills and on the central speed range (1300–1520 rpm) but differ in the choice between HSS-R and HSS-G and in the feed (0.10 vs. 0.20 mm/rev); the difference in objective value is small, since HSS-G at 1520 rpm/0.1 mm/rev (D = 0.852) lies only 0.015 below the measured optimum. The RSM reproduces the responses of the tested condition nearest to its optimum (HSS-R, 1520 rpm, 0.1 mm/rev) for T_{max}, $|BH_{out}|$ and BRout but underestimates F_{max} (36.5 vs. 39.1 N) and T_w (25.6 vs. 27.4 °C), and it fails for the best measured condition, predicting $|BH_{out}|$ = 54.6 ± 26.4 µm and BRout = 16.2 ± 9.0% where 1.8 µm and 0.8% were measured and ranking it eighth of 27 (Table S4). Across the 27 conditions, the Spearman correlation between predicted and measured D is 0.71 ($p < 0.001$): the RSM captures the general pattern of the objective but not its detailed ranking, and because its optimum lies on the feed boundary, it cannot locate an interior optimum. The recommendation is therefore based on the optimisation of the

measured grid; the RSM candidates are reported only as an exploratory comparison, and the RSM provides the trends in Table 7 and confirms the region around the central speed.

3.6.5. Sensitivity and Robustness

Table 9 shows the effect of the weighting. The measured optimum (HSS-G, 1520 rpm, 0.2 mm/rev) is retained with equal weights (W2) and with edge-dominated weights (W3, W5), and it is replaced by carbide at 715 rpm/0.1 mm/rev (D = 0.816) only when the thermo-mechanical responses are weighted five times more than the edge responses (W4), where its low drill and workpiece temperatures outweigh the burr. The RSM optimum is less stable in drill type and speed (HSS-R or HSS-G at 945–2595 rpm) but always lies on the lower feed boundary, again revealing the weakness of the edge models. Because the chip-clogged condition sets the upper limits of both edge responses (Table 6), the measured ranking was also repeated with alternative limits (Table 9, scenarios L1–L2b). Removing this condition and recalculating the limits from the remaining 78 observations (L1) lowered the upper limits to 148.5 µm and 40.5%; fixing them at 100 µm and 30% (L2a) or 50 µm and 20% (L2b) imposed stricter acceptance levels. In all three cases, HSS-G at 1520 rpm and 0.2 mm/rev remained the optimum (D = 0.865, 0.864 and 0.861), followed by the same drill and speed at 0.1 and 0.3 mm/rev. The margin to the second rank increased from 0.015 to 0.028, 0.046 and 0.113, whereas the carbide drill at 715 rpm/0.1 mm/rev fell from rank 4 to ranks 9, 16 and 20. Narrower limits can only reduce the individual desirabilities, and the optimum lies at the lower limit of |BH_(out)|, so the recommendation does not depend on the chip-clogged condition or on the choice of limits.

Table 9. Weight scenarios (weights in the order F_{max}, T_w, T_{max}, $|BH_{out}|$, BR_{out}; W1 = baseline) and the corresponding optima. Grid A: drill speed (rpm) and feed (mm/rev) with measured *D*; Grid B: RSM-grid optimum with predicted *D*. L1–L2b: baseline weights with alternative upper desirability limits of $|BH_{out}|$ and BR_{out} (Section 3.6.5).

Scenario	Weights	Grid A (Optimum)	*D*	Grid B Best Candidate (RSM, Exploratory)	*D*
W1	(3, 3, 3, 5, 5)	HSS-G, 1520, 0.2	0.867	HSS-R, 1325, 0.100	0.814
W2	(1, 1, 1, 1, 1)	HSS-G, 1520, 0.2	0.836	HSS-G, 1125, 0.100	0.793
W3	(1, 1, 1, 5, 5)	HSS-G, 1520, 0.2	0.931	HSS-R, 1650, 0.100	0.891
W4	(5, 5, 5, 1, 1)	Carbide, 715, 0.1	0.816	HSS-G, 945, 0.100	0.763
W5	(0, 0, 0, 1, 1)	HSS-G, 1520, 0.2	0.995	HSS-R, 2595, 0.100	0.999
L1	W1; chip-clogged condition removed; U = 148.5 µm, 40.5%	HSS-G, 1520, 0.2	0.865	-	-
L2a	W1; U fixed at 100 µm, 30%	HSS-G, 1520, 0.2	0.864	-	-
L2b	W1; U fixed at 50 µm, 20%	HSS-G, 1520, 0.2	0.861	-	-

In a stratified bootstrap [98] (1000 resamples of the replicates within each condition), HSS-G/1520 rpm/0.2 mm/rev ranked first in every resample, and the refitted RSM selected HSS-R at about 1325 rpm and 0.1 mm/rev in 98.9% of the resamples (HSS-G at about 1285 rpm in 1.1%; standard deviation of the speed 24 rpm). This stability should not be over-interpreted, because the resampling reflects only the variation between the three replicates of each condition and not the hole-to-hole, sheet-to-sheet and tool-to-tool variation of a confirmation experiment. As a partial test of the hole-to-hole variability, the ranking

according to desirability was also redone using the values for the individual holes from the first series (Table 2), where each condition is represented by one hole without averaging over the replicates (limits Li and Ui based on the 27 holes; weights as in Table 6; Table S5). The three holes drilled with HSS-G at 1520 rpm occupy the first, second, and seventh positions (E33, D = 0.818; E27, D = 0.815; E21, D = 0.786) and, according to the limits given in Table 6, the first, third, and fourth, while the best carbide hole occupies the eighth position in both cases. Thus, the preference for the HSS-G drill at the intermediate drilling speed is confirmed at the hole-to-hole level. However, the ranking of feeds within this group differs from that in Table 3: the seven best holes are in the range ΔD = 0.032, similar to the hole-to-hole variability.

3.7. Practical Recommendations and Limitations

The hole-by-hole results (Sections 3.1–3.5) and the replicated contribution analysis and optimisation (Section 3.6) lead to the following guidelines for dry drilling of GLARE 3-3/2 on conventional machine tools. (1) The ground HSS drill is the most balanced choice: it produced the lowest thrust, nominal-size holes at both faces, the flattest entry edges and small, reproducible exit burrs, and it occupies the first three ranks of the desirability optimisation. At 1520 rpm (28.7 m/min), a feed of 0.2 mm/rev gives the highest desirability (D = 0.867) and twice the feed velocity of 0.1 mm/rev (304 vs. 152 mm/min), which is an almost equal alternative (D = 0.852). Its only failure mode was chip packing at 0.2 mm/rev, and the two extreme speeds (E9, E45), which peck drilling or chip-evacuation monitoring can prevent. (2) The rolled HSS drill is not recommended where the entry-diameter tolerance or the hole integrity matters, because it produces a 0.2–0.5 mm bell mouth and promotes fibre pull-out, matrix chipping and local interface debonding; if it is used, 3030 rpm reduces both entry roll-over and exit burr. (3) The carbide-tipped drill gives the most accurate and roundest holes and the cleanest walls, but it must be run at 3030 rpm and ≤0.2 mm/rev to avoid 60–150 µm exit burrs at 1520 rpm or 0.3 mm/rev; because of its higher thrust and workpiece temperature, it is overall less desirable than the HSS drills unless the thermo-mechanical responses are weighted much more heavily than the edge responses (scenario W4). (4) The feed should not exceed 0.2 mm/rev with HSS drills, since the drill temperature exceeded 110 °C at 0.3 mm/rev for all drills. In summary, drill type sets the thermo-mechanical load (52% of F_{max}, 36% of T_w), feed sets the drill temperature (46%) and the edge quality depends on the drill-specific speed–feed combination. These recommendations for thin 3-3/2 laminates are consistent with the findings of Giasin et al. [34,35] and Park et al. [44] for thicker GLARE grades.

Several limitations apply. (a) The hole-by-hole ANOVA (Table 3) used a single series with the three-factor interaction as the error term and therefore had little power for small effects, and each face was scanned once. (b) The edge responses do not follow smooth response surfaces, so the recommended condition rests on direct measurement and on its stability across the weight scenarios rather than on the model. The recommended condition has not yet been confirmed by an independent experiment. Confirmation drilling at the recommended condition and at less favourable conditions, followed by open-hole tensile tests (ASTM D5766), is planned as a follow-up study. (c) The desirability limits were taken from the observed ranges, which the chip-clogged condition (HSS-G, 715 rpm, 0.2 mm/rev) widened for the edge responses; 21 of the 27 conditions therefore have a $|BH_{out}|$ desirability above 0.8 (20 for BRout), which compresses the differences between acceptable conditions. Recalculating these limits without the chip-clogged condition or fixing them at stricter levels did not change the optimum (Table 9). (d) Chip packing occurred for HSS-G at 0.2 mm/rev at both extreme speeds, and the recommended condition lies between them, so its freedom from chip packing must be confirmed. (e) The replicate scatter is extremely

small (error 0.02–0.03% of the variance in BH_{out} and BRout; maximum replicate spread for BH_{out} = 4.4 µm), and it is much smaller than the hole-to-hole scatter usually reported for burrs produced by drilling. Such scatter is mainly due to the reproducibility of the process of drilling and measurement in the within-batch condition rather than inter-tool-lot variation, panel differences, or different machine settings. Therefore, the *p*-values in Table 5 and the bootstrap stability in Section 3.6.5 might be overestimations in terms of statistical confidence; the results have been obtained based on the effects which govern both replicated and non-replicated results and the single-hole validation test in Section 3.6.5. Confirmation tests using drills from different batches, samples from different panels, and newly drilled holes (including confirmation of the proposed window for chip loading) are needed as follow-up work. (f) The SEM study was qualitative, covered 12 of the 27 holes and excluded the HSS-G drill. (g) Torque and tool wear were not measured, and the optimum applies to the drill diameters, the 2.55 mm laminate and the bench drilling machine used. The aperture and edge-band metrics, however, are automatic and threshold-free and can be applied to any through-hole scan; their extension to diameters verified by a coordinate measuring machine (CMM), coated drills and confirmation experiments is in progress. Recalculating these limits without the chip-clogged condition or fixing them at stricter levels did not change the optimum (Table 9).

4. Conclusions

Dry drilling of autoclave-cured GLARE 3-3/2 laminates with rolled HSS, ground HSS and carbide-tipped drills was studied in a 3^3 full factorial design with thrust-force, infrared-temperature and profilometric measurements of every hole, SEM of the sectioned walls, contribution analysis of replicated data and multi-objective desirability optimisation of the measured conditions supported by RSM. Drill type was the only significant factor for the thrust force (29.6% contribution; 33.3 N for HSS-G, 36.9 N for HSS-R and 39.5 N for carbide), whereas feed governed the maximum drill temperature (101.5–114.6 °C from 0.1 to 0.3 mm/rev) irrespective of drill type, and the workpiece temperature did not exceed 43.4 °C.

Exit burrs, not entry damage, were the dominant edge defect (mean burr height −3.9 µm at entry vs. +25.7 µm at exit; $p < 0.001$). The ground HSS drill produced holes closest to the nominal size (within ±0.04 mm), the flattest entry faces and the smallest exit bulging ratio (3.7%, excluding the chip-clogged hole E9); the rolled HSS drill produced bell-mouthed entries (+0.30 ± 0.17 mm) and the most entry roll-over; the carbide drill produced the most accurate holes but the largest exit burrs (up to 152 µm) at 1520 rpm or 0.3 mm/rev, which vanished at 3030 rpm. Chip clogging of the ground HSS drill at 715 rpm/0.2 mm/rev (E9) produced a 245 µm exit burr, showing that chip evacuation can override the nominal parameters. SEM showed that the rolled HSS drill removes the glass plies by fibre pull-out and damages the adhesive interlayers by matrix chipping, aluminium smearing and debonding, whereas the carbide drill shears the fibres transversely and leaves continuous walls with local aluminium smearing and fibre crushing; the ranking of the two drills therefore reverses between the hole face and the hole wall.

In the replicated data set (81 holes), drill type contributed 52% of the variation of F_{max} and 36% of T_w, feed contributed 46% of T_{max}, and two- and three-factor interactions explained 72–87% of the variation of BH_{out} and BRout. The ground HSS drill at 1520 rpm and 0.2 mm/rev was the best compromise (D = 0.867; F_{max} = 31.1 N, T_{max} = 102.5 °C, $|BH_{out}|$ = 1.8 µm, BRout = 0.8%) and remained so under alternative desirability limits, under all weightings except the thermo-mechanically dominated scenario W4, and under bootstrap resampling; at the level of drill type and spindle speed, this preference was also

reproduced by the single-hole values of the first series. Because the RSM described only the thermo-mechanical responses, the recommendation is based on the measured grid.

For burr-free, dimensionally accurate dry drilling of GLARE 3-3/2 on conventional machines, a ground HSS drill at 1520 rpm and 0.1–0.2 mm/rev with chip control is recommended, or a carbide-tipped drill at 3030 rpm and ≤0.2 mm/rev where dimensional accuracy has priority; rolled HSS drills should be avoided where the entry-diameter tolerance matters. Since the replicate scatter represents within-batch reproducibility and not process variability, this recommendation can be accepted at the drill and spindle speed level, but not at the feed level itself, and separate verification experiments should be performed with drills of different batches, panels of different pieces, and newly drilled holes.

Supplementary Materials: The following supporting information can be downloaded at: https://www.mdpi.com/article/10.3390/polym18222850/s1. Supplementary Note S1: infrared thermograms at drill withdrawal; Supplementary Note S2: instrument-reported hole and peak areas; Figure S1: main-effect plots of the mean thrust force and the maximum drill temperature; Figure S2: infrared thermograms at drill withdrawal; Figure S3: aperture oversize and out-of-roundness; Figure S4: instrument-reported hole and peak areas; Figure S5: exit burr height and bulging ratio vs. thrust force and drill temperature; Figure S6: contributions of the model terms to the total sum of squares; Figure S7: workflow of the contribution analysis and optimisation; Figure S8: composite desirability over the refined grid; Figure S9: ranked composite desirability of the 27 conditions and individual desirabilities; Table S1: condition means, composite desirability and rank of the 27 conditions; Table S2: control parameters of the RSM–desirability–grid-search optimisation; Table S3: statistics of the pooled second-order RSM models; Table S4: measured and RSM-predicted responses at the measured and RSM optima. Table S5: composite desirability and rank of the 27 single holes of the first series. Table S6: treatment of the chip-packed holes E9 and E45 in each analysis. Table S7: sensitivity of the bulging ratio and depressed fraction to the height threshold; Figure S10: exit bulging ratio and entry depressed fraction of the three drills as functions of the height threshold.

Author Contributions: Conceptualisation, S.F. and S.Ü.; methodology, S.F.; investigation, Ö.Ç.Ç.; resources, M.Ö.B. and E.Y.; data curation, Ö.Ç.Ç. and S.Ü.; formal analysis, S.F.; validation, M.İ.Ö. and E.Y.; visualisation, S.F.; writing—original draft preparation, Ö.Ç.Ç. and S.F.; writing—review and editing, S.Ü., M.Ö.B., M.İ.Ö., E.Y. and S.F.; supervision, S.F. All authors have read and agreed to the published version of the manuscript.

Funding: This work was supported by the Kocaeli University Scientific Research Projects Coordination Unit [Project No: FBA-2026-5449].

Institutional Review Board Statement: Not applicable.

Data Availability Statement: The thrust-force, temperature and profilometric data supporting the findings of this study are available from the corresponding author upon reasonable request.

Acknowledgments: The authors thank the Kocaeli University Wear Laboratory for the profilometric measurements.

Conflicts of Interest: The authors declare no conflicts of interest.

Abbreviations

The following abbreviations are used in this manuscript:

ANOVA	analysis of variance
BES	backscattered-electron (imaging)
BH	burr height
BMS	Boeing Material Specification
BR	bulging ratio
CARALL	carbon-fibre-reinforced aluminium laminate
CFRP	carbon-fibre-reinforced polymer

CMM	coordinate measuring machine
CNC	computer numerical control
CV	coefficient of variation
D	composite desirability
d.f.	degrees of freedom
DF	depressed fraction
FML	fibre metal laminate
FRP	fibre-reinforced polymer
GFRP	glass-fibre-reinforced polymer
GLARE	glass laminate aluminium reinforced epoxy
HSS	high-speed steel
HSS-Co	cobalt high-speed steel
HSS-G	ground high-speed-steel drill
HSS-R	rolled high-speed-steel drill
PC	percentage contribution
RSM	response surface methodology
S	weighted-sum score
SEI	secondary-electron imaging
SEM	scanning electron microscopy
SRM	Structural Repair Manual
F_{mean}, F_{max}	mean and maximum thrust force
T_w, T_{chip}, T_{max}	workpiece, chip and maximum drill temperature
D_{eq}	equivalent aperture diameter
n	spindle speed
f	Feed

References

1. Sinmazçelik, T.; Avcu, E.; Bora, M.Ö.; Çoban, O. A review: Fibre metal laminates, background, bonding types and applied test methods. *Mater. Des.* **2011**, *32*, 3671–3685. [CrossRef]
2. Vermeeren, C.A.J.R. An Historic Overview of the Development of Fibre Metal Laminates. *Appl. Compos. Mater.* **2003**, *10*, 189–205. [CrossRef]
3. Vogelesang, L.B.; Vlot, A. Development of fibre metal laminates for advanced aerospace structures. *J. Mater. Process. Technol.* **2000**, *103*, 1–5. [CrossRef]
4. Gunnink, J.W.; Vlot, A.; de Vries, T.J.; van der Hoeven, W. Glare Technology Development 1997–2000. *Appl. Compos. Mater.* **2002**, *9*, 201–219. [CrossRef]
5. Vlot, A.; Gunnink, J.W. (Eds.) *Fibre Metal Laminates*; Kluwer Academic Publishers: Dordrecht, The Netherlands, 2001. [CrossRef]
6. Alderliesten, R.C.; Hagenbeek, M.; Homan, J.J.; Hooijmeijer, P.A.; de Vries, T.J.; Vermeeren, C.A.J.R. Fatigue and Damage Tolerance of Glare. *Appl. Compos. Mater.* **2003**, *10*, 223–242. [CrossRef]
7. Wu, G.; Yang, J.-M. The mechanical behavior of GLARE laminates for aircraft structures. *JOM* **2005**, *57*, 72–79. [CrossRef]
8. Asundi, A.; Choi, A.Y.N. Fiber metal laminates: An advanced material for future aircraft. *J. Mater. Process. Technol.* **1997**, *63*, 384–394. [CrossRef]
9. Sinke, J. Manufacturing of GLARE Parts and Structures. *Appl. Compos. Mater.* **2003**, *10*, 293–305. [CrossRef]
10. Caggiano, M.; Saffioti, M.R.; Rotella, G. Fiber Metal Laminates: The Role of the Metal Surface and Sustainability Aspects. *J. Compos. Sci.* **2025**, *9*, 35. [CrossRef]
11. Costa, R.D.F.S.; Sales-Contini, R.C.M.; Silva, F.J.G.; Sebbe, N.; Jesus, A.M.P. A Critical Review on Fiber Metal Laminates (FML): From Manufacturing to Sustainable Processing. *Metals* **2023**, *13*, 638. [CrossRef]
12. Franz, G.; Vantomme, P.; Hassan, M.H. A Review on Drilling of Multilayer Fiber-Reinforced Polymer Composites and Aluminum Stacks: Optimization of Strategies for Improving the Drilling Performance of Aerospace Assemblies. *Fibers* **2022**, *10*, 78. [CrossRef]
13. Slamani, M.; Chatelain, J.-F. A review on the machining of polymer composites reinforced with carbon (CFRP), glass (GFRP), and natural fibers (NFRP). *Discov. Mech. Eng.* **2023**, *2*, 4. [CrossRef]
14. Rahme, P. A bibliometric analysis on drilling of composite materials using a systematic approach. *Heliyon* **2024**, *10*, e37282. [CrossRef] [PubMed]
15. Jagadeesh, P.; Mavinkere Rangappa, S.; Suyambulingam, I.; Siengchin, S.; Puttegowda, M.; Binoj, J.S.; Gorbatyuk, S.; Khan, A.; Doddamani, M.; Fiore, V.; et al. Drilling characteristics and properties analysis of fiber reinforced polymer composites: A comprehensive review. *Heliyon* **2023**, *9*, e14428. [CrossRef] [PubMed]
16. Gao, T.; Zhang, Y.; Li, C.; Wang, Y.; Chen, Y.; An, Q.; Zhang, S.; Li, H.N.; Cao, H.; Ali, H.M.; et al. Fiber-reinforced composites in milling and grinding: Machining bottlenecks and advanced strategies. *Front. Mech. Eng.* **2022**, *17*, 24. [CrossRef]

17. Geier, N.; Davim, J.P.; Szalay, T. Advanced cutting tools and technologies for drilling carbon fibre reinforced polymer (CFRP) composites: A review. *Compos. Part A Appl. Sci. Manuf.* **2019**, *125*, 105552. [CrossRef]
18. Shetty, N.; Shahabaz, S.M.; Sharma, S.S.; Shetty, S.D. A review on finite element method for machining of composite materials. *Compos. Struct.* **2017**, *176*, 790–802. [CrossRef]
19. Pramanik, A.; Basak, A.K.; Dong, Y.; Sarker, P.K.; Uddin, M.S.; Littlefair, G.; Dixit, A.R.; Chattopadhyaya, S. Joining of carbon fibre reinforced polymer (CFRP) composites and aluminium alloys—A review. *Compos. Part A Appl. Sci. Manuf.* **2017**, *101*, 1–29. [CrossRef]
20. Ürgün, S.; Fidan, S.; Yarar, E.; Özsoy, M.İ.; Bora, M.Ö. Thermomechanical Properties of Carbon and Glass Fiber-Reinforced Epoxy Composites as Function of Drilling Parameters. *Polymers* **2026**, *18*, 2316. [CrossRef] [PubMed]
21. Hocheng, H.; Dharan, C.K.H. Delamination During Drilling in Composite Laminates. *J. Eng. Ind.* **1990**, *112*, 236–239. [CrossRef]
22. Jain, S.; Yang, D.C.H. Effects of Feedrate and Chisel Edge on Delamination in Composites Drilling. *J. Eng. Ind.* **1993**, *115*, 398–405. [CrossRef]
23. Chen, W.-C. Some experimental investigations in the drilling of carbon fiber-reinforced plastic (CFRP) composite laminates. *Int. J. Mach. Tools Manuf.* **1997**, *37*, 1097–1108. [CrossRef]
24. Hocheng, H.; Tsao, C.C. Comprehensive analysis of delamination in drilling of composite materials with various drill bits. *J. Mater. Process. Technol.* **2003**, *140*, 335–339. [CrossRef]
25. Hocheng, H.; Tsao, C.C. Effects of special drill bits on drilling-induced delamination of composite materials. *Int. J. Mach. Tools Manuf.* **2006**, *46*, 1403–1416. [CrossRef]
26. Davim, J.; Rubio, J.; Abrao, A. A novel approach based on digital image analysis to evaluate the delamination factor after drilling composite laminates. *Compos. Sci. Technol.* **2007**, *67*, 1939–1945. [CrossRef]
27. Silva, D.; Pamies Teixeira, J.; Machado, C.M. Methodology analysis for evaluation of drilling-induced damage in composites. *Int. J. Adv. Manuf. Technol.* **2014**, *71*, 1919–1928. [CrossRef]
28. Babu, J.; Sunny, T.; Paul, N.A.; Mohan, K.P.; Philip, J.; Davim, J.P. Assessment of delamination in composite materials: A review. *Proc. Inst. Mech. Eng. Part B J. Eng. Manuf.* **2016**, *230*, 1990–2003. [CrossRef]
29. Geng, D.; Liu, Y.; Shao, Z.; Lu, Z.; Cai, J.; Li, X.; Jiang, X.; Zhang, D. Delamination formation, evaluation and suppression during drilling of composite laminates: A review. *Compos. Struct.* **2019**, *216*, 168–186. [CrossRef]
30. Qiu, X.; Li, P.; Li, C.; Niu, Q.; Chen, A.; Ouyang, P.; Ko, T.J. Study on chisel edge drilling behavior and step drill structure on delamination in drilling CFRP. *Compos. Struct.* **2018**, *203*, 404–413. [CrossRef]
31. Giasin, K.; Ayvar-Soberanis, S.; Hodzic, A. An experimental study on drilling of unidirectional GLARE fibre metal laminates. *Compos. Struct.* **2015**, *133*, 794–808. [CrossRef]
32. Giasin, K.; Ayvar-Soberanis, S. An Investigation of burrs, chip formation, hole size, circularity and delamination during drilling operation of GLARE using ANOVA. *Compos. Struct.* **2017**, *159*, 745–760. [CrossRef]
33. Giasin, K.; Ayvar-Soberanis, S.; French, T.; Phadnis, V. 3D Finite Element Modelling of Cutting Forces in Drilling Fibre Metal Laminates and Experimental Hole Quality Analysis. *Appl. Compos. Mater.* **2017**, *24*, 113–137. [CrossRef]
34. Giasin, K.; Gorey, G.; Byrne, C.; Sinke, J.; Brousseau, E. Effect of machining parameters and cutting tool coating on hole quality in dry drilling of fibre metal laminates. *Compos. Struct.* **2019**, *212*, 159–174. [CrossRef]
35. Giasin, K.; Hawxwell, J.; Sinke, J.; Dhakal, H.; Köklü, U.; Brousseau, E. The effect of cutting tool coating on the form and dimensional errors of machined holes in GLARE® fibre metal laminates. *Int. J. Adv. Manuf. Technol.* **2020**, *107*, 2817–2832. [CrossRef]
36. Giasin, K.; Dad, A.; Brousseau, E.; Pimenov, D.; Mia, M.; Morkavuk, S.; Koklu, U. The effects of through tool cryogenic machining on the hole quality in GLARE® fibre metal laminates. *J. Manuf. Process.* **2021**, *64*, 996–1012. [CrossRef]
37. Giasin, K.; Ayvar-Soberanis, S.; Hodzic, A. Evaluation of cryogenic cooling and minimum quantity lubrication effects on machining GLARE laminates using design of experiments. *J. Clean. Prod.* **2016**, *135*, 533–548. [CrossRef]
38. Giasin, K.; Atif, M.; Ma, Y.; Jiang, C.; Koklu, U.; Sinke, J. Machining GLARE fibre metal laminates: A comparative study on drilling effect between conventional and ultrasonic-assisted drilling. *Int. J. Adv. Manuf. Technol.* **2022**, *123*, 3657–3672. [CrossRef]
39. Pawar, O.A.; Gaikhe, Y.S.; Tewari, A.; Sundaram, R.; Joshi, S.S. Analysis of hole quality in drilling GLARE fiber metal laminates. *Compos. Struct.* **2015**, *123*, 350–365. [CrossRef]
40. Akula, S.; Bolar, G. Comparative evaluation of machining processes for making holes in GLARE fiber metal laminates. *Mater. Today Proc.* **2021**, *46*, 9126–9131. [CrossRef]
41. Tyczyński, P.; Lemańczyk, J.; Ostrowski, R.; Śliwa, R.E. Drilling of CFRP, GFRP, glare type composites. *Aircr. Eng. Aerosp. Technol.* **2014**, *86*, 312–322. [CrossRef]
42. Sorrentino, L.; Turchetta, S.; Parodo, G. Drilling of glare laminates: Effect of cutting parameters on process forces and temperatures. *Int. J. Adv. Manuf. Technol.* **2022**, *120*, 645–657. [CrossRef]
43. Boughdiri, I.; Giasin, K.; Mabrouki, T.; Zitoune, R. Effect of cutting parameters on thrust force, torque, hole quality and dust generation during drilling of GLARE 2B laminates. *Compos. Struct.* **2021**, *261*, 113562. [CrossRef]

44. Park, S.Y.; Choi, W.J.; Choi, C.H.; Choi, H.S. Effect of drilling parameters on hole quality and delamination of hybrid GLARE laminate. *Compos. Struct.* **2018**, *185*, 684–698. [CrossRef]
45. Ekici, E.; Motorcu, A.R.; Yıldırım, E. An experimental study on hole quality and different delamination approaches in the drilling of CARALL, a new FML composite. *FME Trans.* **2021**, *49*, 950–961. [CrossRef]
46. Ekici, E.; Motorcu, A.R.; Uzun, G. Multi-objective optimization of process parameters for drilling fibermetal laminate using a hybrid GRA-PCA approach. *FME Trans.* **2021**, *49*, 356–366. [CrossRef]
47. Ekici, E.; Pazarkaya, İ.; Uzun, G. Delamination and thrust force analysis in GLARE: Influence of tool geometry and prediction with machine learning models. *J. Compos. Mater.* **2025**, *59*, 1233–1249. [CrossRef]
48. Mohan, N.; Kalam, S.A.; Mahaveerakannan, R.; Shah, M.; Yadav, J.S.; Sharma, V.; Naik, P.S.; Bharathi Narasimha, D. Statistical Evaluation of Machining Parameters in Drilling of Glass Laminate Aluminum Reinforced Epoxy Composites using Machine Learning Model. *Eng. Sci.* **2022**, *20*, 244–251. [CrossRef]
49. Atif, M.; Wang, X.; Xie, L.; Sun, T.; Giasin, K.; Ma, Y. Influence of cutting tool design on ultrasonic-assisted drilling of fiber metal laminates. *Int. J. Adv. Manuf. Technol.* **2024**, *131*, 6039–6059. [CrossRef]
50. Atif, M.; Wang, X.; Xie, L.; Giasin, K.; Ma, Y.; Jiang, C.; Koklu, U.; Sinke, J. Multiscale modelling and experimental analysis of ultrasonic-assisted drilling of GLARE fibre metal laminates. *Compos. Part A Appl. Sci. Manuf.* **2024**, *177*, 107962. [CrossRef]
51. Logesh, K.; Moshi, A.A.M.; Bharathi, S.R.S.; Hariharasakthisudhan, P. A multi-objective grey relational approach and regression analysis on optimization of drilling process parameters for GLARE fiber metal laminates. *Surf. Rev. Lett.* **2022**, *29*, 2250066. [CrossRef]
52. Bolar, G.; Dinesh, A.A.; Polishetty, A.; Shetty, R.; Hiremath, A.; Neelakantha, V.L. Performance Analysis of Helical Milling and Drilling Operations While Machining Carbon Fiber-Reinforced Aluminum Laminates. *J. Manuf. Mater. Process.* **2024**, *8*, 113. [CrossRef]
53. Sourd, X.; Giasin, K.; Zitoune, R.; Salem, M.; Lupton, C. Multi-scale analysis of the damage and contamination in abrasive water jet drilling of GLARE fibre metal laminates. *J. Manuf. Process.* **2022**, *84*, 610–621. [CrossRef]
54. Reddy, V.N.; Venkatesh, B. Optimization of parameters in abrasive water jet machining of glass laminate aluminium reinforced epoxy (GLARE). *Mater. Today Proc.* **2019**, *19*, 890–894. [CrossRef]
55. Hariharasakthisudhan, P.; Logesh, K.; Kannan, S.; Sivakumar, R.; Sathickbasha, K. Optimizing the process parameter of abrasive water jet machining against sub-surface delamination of nanoclay modified GLARE laminates. *Surf. Rev. Lett.* **2025**, *32*, 2550086. [CrossRef]
56. Giasin, K.; Ayvar-Soberanis, S. Evaluation of Workpiece Temperature during Drilling of GLARE Fiber Metal Laminates Using Infrared Techniques: Effect of Cutting Parameters, Fiber Orientation and Spray Mist Application. *Materials* **2016**, *9*, 622. [CrossRef] [PubMed]
57. Leonidas, E.; Ayvar-Soberanis, S.; Laalej, H.; Fitzpatrick, S.; Willmott, J.R. A Comparative Review of Thermocouple and Infrared Radiation Temperature Measurement Methods during the Machining of Metals. *Sensors* **2022**, *22*, 4693. [CrossRef] [PubMed]
58. Merino-Pérez, J.L.; Royer, R.; Ayvar-Soberanis, S.; Merson, E.; Hodzic, A. On the temperatures developed in CFRP drilling using uncoated WC-Co tools Part I: Workpiece constituents, cutting speed and heat dissipation. *Compos. Struct.* **2015**, *123*, 161–168. [CrossRef]
59. Merino-Pérez, J.L.; Hodzic, A.; Merson, E.; Ayvar-Soberanis, S. On the temperatures developed in CFRP drilling using uncoated WC-Co tools Part II: Nanomechanical study of thermally aged CFRP composites. *Compos. Struct.* **2015**, *123*, 30–34. [CrossRef]
60. Fu, R.; Jia, Z.; Wang, F.; Jin, Y.; Sun, D.; Yang, L.; Cheng, D. Drill-exit temperature characteristics in drilling of UD and MD CFRP composites based on infrared thermography. *Int. J. Mach. Tools Manuf.* **2018**, *135*, 24–37. [CrossRef]
61. Wang, F.-J.; Yin, J.-W.; Ma, J.-W.; Niu, B. Heat partition in dry orthogonal cutting of unidirectional CFRP composite laminates. *Compos. Struct.* **2018**, *197*, 28–38. [CrossRef]
62. Box, G.E.P.; Wilson, K.B. On the Experimental Attainment of Optimum Conditions. *J. R. Stat. Soc. Ser. B Methodol.* **1951**, *13*, 1–38. [CrossRef]
63. Myers, R.H.; Montgomery, D.C.; Anderson-Cook, C.M. *Response Surface Methodology: Process and Product Optimization Using Designed Experiments*, 4th ed.; Wiley: Hoboken, NJ, USA, 2016.
64. Derringer, G.; Suich, R. Simultaneous Optimization of Several Response Variables. *J. Qual. Technol.* **1980**, *12*, 214–219. [CrossRef]
65. Thakre, A.A.; Soni, S. Modeling of burr size in drilling of aluminum silicon carbide composites using response surface methodology. *Eng. Sci. Technol. Int. J.* **2016**, *19*, 1199–1205. [CrossRef]
66. Shanmughasundaram, P.; Subramanian, R. Study of parametric optimization of burr formation in step drilling of eutectic Al–Si alloy–Gr composites. *J. Mater. Res. Technol.* **2014**, *3*, 150–157. [CrossRef]
67. Kilickap, E. Optimization of cutting parameters on delamination based on Taguchi method during drilling of GFRP composite. *Expert Syst. Appl.* **2010**, *37*, 6116–6122. [CrossRef]
68. Davim, J.P.; Reis, P. Study of delamination in drilling carbon fiber reinforced plastics (CFRP) using design experiments. *Compos. Struct.* **2003**, *59*, 481–487. [CrossRef]

69. Ünüvar, A.; Öztürk, O. Machinability analysis of delamination and thrust force in drilling of pure and added GFRP composites. *J. Compos. Mater.* **2022**, *57*, 3–21. [CrossRef]
70. Arul, S.; Samuel Raj, D.; Vijayaraghavan, L.; Malhotra, S.K.; Krishnamurthy, R. Modeling and Optimization of Process Parameters for Defect Toleranced Drilling of GFRP Composites. *Mater. Manuf. Process.* **2006**, *21*, 357–365. [CrossRef]
71. Verma, R.K.; Pal, P.K.; Kandpal, B.C. Machining performance optimization in drilling of GFRP composites: A utility theory (UT) based approach. In Proceedings of the 2016 International Conference on Control, Computing, Communication and Materials (ICCCCM), Allahabad, India, 21–22 October 2016; IEEE: New York, NY, USA, 2016; pp. 1–5. [CrossRef]
72. Wang, Q.; Jia, X. Optimization of cutting parameters for improving exit delamination, surface roughness, and production rate in drilling of CFRP composites. *Int. J. Adv. Manuf. Technol.* **2021**, *117*, 3487–3502. [CrossRef]
73. Kiliçkap, E.; Yardimeden, A.; Çelik, Y.H. Investigation of experimental study of end milling of CFRP composite. *Sci. Eng. Compos. Mater.* **2015**, *22*, 89–95. [CrossRef]
74. Pascual, V.; San-Juan, M.; Santos, F.J.; Martín, Ó.; de Tiedra, M.P. Study of axial cutting forces and delamination phenomenon in drilling of carbon fiber composites. *Procedia Manuf.* **2017**, *13*, 67–72. [CrossRef]
75. Kumar, J.; Verma, R.K. Delamination assessment during machining of laminated polymer nanocomposite. *Int. J. Mod. Manuf. Technol.* **2021**, *13*, 109–115. [CrossRef]
76. Nikam, M.; Al-Lohedan, H.A.; Mohammad, F.; Khetree, S.; Patil, V.; Lonare, G.; Khan, F.J.; Jagatap, G.; Giri, J.P.; Oza, A.D.; et al. Optimization of Machining Parameters for Enhanced Performance of Glass-Fibre-Reinforced Plastic (GFRP) Composites Using Design of Experiments. *Sustainability* **2023**, *15*, 12372. [CrossRef]
77. Jenarthanan, M.P.; Nishanth, G.; Bharathwaj, R. Optimization of machining parameters in end milling of GFRP composites based on the Taguchi method with fuzzy logics. *Int. J. Knowl.-Based Intell. Eng. Syst.* **2016**, *20*, 123–134. [CrossRef]
78. Jenarthanan, M.P.; Jeyapaul, R. Optimisation of machining parameters on milling of GFRP composites by desirability function analysis using Taguchi method. *Int. J. Eng. Sci. Technol.* **2018**, *5*, 22–36. [CrossRef]
79. Palanikumar, K.; Karunamoorthy, L.; Karthikeyan, R. Multiple Performance Optimization of Machining Parameters on the Machining of GFRP Composites Using Carbide (K10) Tool. *Mater. Manuf. Process.* **2006**, *21*, 846–852. [CrossRef]
80. Hussain, S.A.; Pandurangadu, V.; Kumar, K.P. Machining parameters optimisation in turning of GFRP composites by desirability function analysis embedded with Taguchi method. *Int. J. Mach. Mach. Mater.* **2015**, *17*, 95. [CrossRef]
81. Bahei El-Deen, A. Multi optimization in slot milling of CFRP composites through grey relational-based Taguchi analysis. *Niger. J. Technol. Dev.* **2024**, *21*, 11–18. [CrossRef]
82. Ducobu, F.; Mélice, E.; Rivière-Lorphèvre, E.; Beuscart, T.; Aizpuru, O.; Granjon, A.; Flores, P.; Soriano, D.; Cuesta, M.; Arrazola, P.-J. Sensitivity Analysis of Various Geometries of PCD and Cemented Tungsten Carbide Cutting Tools during the Milling of GFRP Composite. *Polymers* **2022**, *14*, 1524. [CrossRef] [PubMed]
83. Raj, P.P.; Perumal, A.E. Taguchi Analysis of surface roughness and delamination associated with various cemented carbide K10 end mills in milling of GFRP. *J. Eng. Sci. Technol. Rev.* **2010**, *3*, 58–64. [CrossRef]
84. Nurhaniza, M.; Ariffin, M.K.A.M.; Mustapha, F.; Baharudin, B.T.H.T. Analyzing the Effect of Machining Parameters Setting to the Surface Roughness during End Milling of CFRP-Aluminium Composite Laminates. *Int. J. Manuf. Eng.* **2016**, *2016*, 1–9. [CrossRef]
85. Doluk, E.; Rudawska, A. Effect of Machining Settings and Tool Geometry on Surface Quality After Machining of Al/CFRP Sandwich Structures. *Adv. Sci. Technol. Res. J.* **2022**, *16*, 22–33. [CrossRef] [PubMed]
86. Doluk, E.; Rudawska, A.; Miturska-Barańska, I. Investigation of the Surface Roughness and Surface Uniformity of a Hybrid Sandwich Structure after Machining. *Materials* **2022**, *15*, 7299. [CrossRef] [PubMed]
87. Fernández-Pérez, J.; Cantero, J.L.; Díaz-Álvarez, J.; Miguélez, M.H. Hybrid Composite-Metal Stack Drilling with Different Minimum Quantity Lubrication Levels. *Materials* **2019**, *12*, 448. [CrossRef] [PubMed]
88. Hamedanianpour, H.; Chatelain, J.F. Effect of Tool Wear on Quality of Carbon Fiber Reinforced Polymer Laminate during Edge Trimming. *Appl. Mech. Mater.* **2013**, *325–326*, 34–39. [CrossRef]
89. Ozkan, D.; Panjan, P.; Gok, M.S.; Karaoglanli, A.C. Experimental Study on Tool Wear and Delamination in Milling CFRPs with TiAlN- and TiN-Coated Tools. *Coatings* **2020**, *10*, 623. [CrossRef]
90. Sun, Z.; Geng, D.; Zheng, W.; Liu, Y.; Liu, L.; Ying, E.; Jiang, X.; Zhang, D. An innovative study on high-performance milling of carbon fiber reinforced plastic by combining ultrasonic vibration assistance and optimized tool structures. *J. Mater. Res. Technol.* **2023**, *22*, 2131–2146. [CrossRef]
91. İç, Y.T.; Elaldı, F.; Keçeci, B.; Önder Uzun, G.; Limoncuoğlu, N.; Aksoy, İ. Kevlar fiber-epoksi kompozit malzemesinin frezeleme işleminin faktöriyel tasarım ve hedef programlama yöntemleriyle eniyilemesi (Optimization of milling parameters of Kevlar fiber–epoxy composite by factorial design and goal programming). *Gazi Üniversitesi Mühendis. Mimar. Fakültesi Derg.* **2019**, *34*, 1549–1560. [CrossRef]
92. Alkhafaji, G.M.; Alshammaa, F.A.; Khalid, E.A. Fabricating Different Laminate Composites by Manual Layup and Estimating the Optimum Parameters for CNC Milling Machine. *AL-Nahrain J. Eng. Sci.* **2020**, *23*, 388–396. [CrossRef]

93. Nguyen-Dinh, N.; Bouvet, C.; Zitoune, R. Influence of machining damage generated during trimming of CFRP composite on the compressive strength. *J. Compos. Mater.* **2020**, *54*, 1413–1430. [CrossRef]
94. Hexcel Corporation. *HexPly® BMS 8-139 Qualified Prepreg—Product Data Sheet*; Hexcel: Stamford, CT, USA, 2020.
95. Airbus Operations, S.A.S. Chapter 53-15-12: Curing Parameters for GLARE Panels. In *Structural Repair Manual (SRM)*; Airbus: Blagnac, France, 2020.
96. Kim, J.; Min, S.; Dornfeld, D.A. Optimization and control of drilling burr formation of AISI 304L and AISI 4118 based on drilling burr control charts. *Int. J. Mach. Tools Manuf.* **2001**, *41*, 923–936. [CrossRef]
97. *ISO 25178-2:2021*; Geometrical product specifications (GPS)—Surface texture: Areal—Part 2: Terms, definitions and surface texture parameters. International Organization for Standardization: Geneva, Switzerland, 2021.
98. Efron, B.; Tibshirani, R.J. *An Introduction to the Bootstrap*; Chapman & Hall: New York, NY, USA, 1993. [CrossRef]
99. Hwang, C.L.; Yoon, K. *Multiple Attribute Decision Making: Methods and Applications A State-of-the-Art Survey*; Lecture Notes in Economics and Mathematical Systems; Springer: Berlin/Heidelberg, Germany, 1981; Volume 186. [CrossRef]

Disclaimer/Publisher's Note: The statements, opinions and data contained in all publications are solely those of the individual author(s) and contributor(s) and not of MDPI and/or the editor(s). MDPI and/or the editor(s) disclaim responsibility for any injury to people or property resulting from any ideas, methods, instructions or products referred to in the content.